



# Multiwavelength Analysis of A1240, the Double Radio-relic Merging Galaxy Cluster Embedded in an $\sim 80$ Mpc-long Cosmic Filament

Hyejeon Cho<sup>1</sup> , M. James Jee<sup>1,2</sup> , Rory Smith<sup>3,4</sup> , Kyle Finner<sup>5,1</sup> , and Wonki Lee<sup>1</sup> <sup>1</sup> Department of Astronomy, Yonsei University, 50 Yonsei-ro, Seodaemun-gu, Seoul 03722, Republic of Korea; [hyejeon@yonsei.ac.kr](mailto:hyejeon@yonsei.ac.kr)<sup>2</sup> Department of Physics and Astronomy, University of California, Davis, One Shields Avenue, Davis, CA 95616, USA; [mjjee@yonsei.ac.kr](mailto:mjjee@yonsei.ac.kr)<sup>3</sup> Korea Astronomy and Space Science Institute (KASI), 776 Daedeokdae-ro, Yuseong-gu, Daejeon 34055, Republic of Korea<sup>4</sup> University of Science and Technology (UST), 217 Gajeong-ro, Yuseong-gu, Daejeon 34113, Republic of Korea<sup>5</sup> Infrared Processing and Analysis Center, California Institute of Technology, Pasadena, CA 91125, USA

Received 2021 September 13; revised 2021 October 25; accepted 2021 November 3; published 2022 January 26

## Abstract

We present a multiwavelength study of the double radio-relic cluster A1240 at  $z = 0.195$ . Our Subaru-based weak-lensing analysis detects three mass clumps forming an  $\sim 4$  Mpc filamentary structure elongated in a north–south orientation. The northern ( $M_{200} = 2.61^{+0.51}_{-0.60} \times 10^{14} M_{\odot}$ ) and middle ( $M_{200} = 1.09^{+0.34}_{-0.43} \times 10^{14} M_{\odot}$ ) mass clumps separated by  $\sim 1.3$  Mpc are associated with A1240 and colocated with the X-ray peaks and cluster galaxy overdensities revealed by Chandra and MMT/Hectospec observations, respectively. The southern mass clump ( $M_{200} = 1.78^{+0.44}_{-0.55} \times 10^{14} M_{\odot}$ ),  $\sim 1.5$  Mpc to the south of the middle clump, coincides with the galaxy overdensity in A1237, the A1240 companion cluster at  $z = 0.194$ . Considering the positions, orientations, and polarization fractions of the double radio relics measured by the LOFAR study, we suggest that A1240 is a postmerger binary system in the returning phase with a time since collision of  $\sim 1.7$  Gyr. With the SDSS DR16 data analysis, we also find that A1240 is embedded in the much larger scale ( $\sim 80$  Mpc) filamentary structure whose orientation is in remarkable agreement with the hypothesized merger axis of A1240.

*Unified Astronomy Thesaurus concepts:* Abell clusters (9); Cosmic web (330); Dark matter (353); Intracluster medium (858); Radio continuum emission (1340); Weak gravitational lensing (1797); X-ray astronomy (1810)

*Supporting material:* machine-readable table

## 1. Introduction

Radio relics, also known as cluster radio shocks, refer to megaparsec-scale diffuse synchrotron radio emission features observed in the outskirts of merging galaxy clusters. Tracing the merger shocks, they provide unique information, such as viewing angle, collision velocity, merger axis, etc., on the merging scenarios that cannot be directly accessed with other wavelength data alone (e.g., Enßlin et al. 1998; see van Weeren et al. 2019 for a recent review and references therein). There is a growing interest in studying radio-relic clusters to understand the formation and evolution of the merger shocks, the mechanism of cosmic-ray particle acceleration, the interaction between plasma turbulence and intracluster magnetic field, etc. In addition, to those who desire to utilize merging clusters as dark matter (DM) laboratories, radio-relic clusters provide powerful environments because the information on their merger histories is more readily available (e.g., Ng et al. 2015; Golovich et al. 2016; Monteiro-Oliveira et al. 2017; Finner et al. 2021).

Double radio relics are a subclass of radio relics that exhibit two relics on opposite sides. The first detection of double relics dates back to 1997, when Röttgering et al. (1997) found two extended diffuse radio sources in the northwest and southeast peripheral regions of A3667 using ATCA and MOST data. Although, in principle, every collision between clusters generates shocks in pairs, observationally, there are only a dozen or so double radio-relic systems reported to date. The

rarity indicates that the merger should perhaps meet some delicate criteria in order to produce two observable radio relics.

Given that our understanding of the exact mechanism in relic creation and particle acceleration is still highly incomplete, the double radio-relic system serves as a powerful test bed for different models because the two relics probe the same merger. In particular, *symmetric*<sup>6</sup> double radio-relic systems are most useful, as they allow us to reduce the complexity in our inference of their merger scenarios. Three well-known examples in this category are PSZ1 G108.18–11.53, MACS 1752.0+4440, and ZWCL 1856.8+6616 (e.g., de Gasperin et al. 2015; Finner et al. 2021).

In this paper, we present a multiwavelength analysis of the cluster merger A1240 at  $z = 0.195$ , which belongs to the Merging Cluster Collaboration (MC<sup>2</sup>) *gold sample* that the Collaboration proposed to follow up on as a priority with more detailed studies including comparisons between their galaxy and mass distributions (Golovich et al. 2019b, hereafter G19b). A1240 is one of the few systems that possess symmetric double relics (Figure 1).

The first suggestion that A1240 might host two radio relics was made by Kempner & Sarazin (2001) based on the WENSS and NVSS radio images. With deep Very Large Array (VLA) observations at 20 cm (1.4 GHz) and 90 cm (325 MHz), Bonafede et al. (2009) confirmed the presence of the two radio relics in A1240 and firmly detected a spectral index flattening toward the cluster outskirts in the northern relic, which is consistent with our expectation if the relic indeed traces the merger shock traveling to the north. For both relics, moderate

Original content from this work may be used under the terms of the [Creative Commons Attribution 4.0 licence](https://creativecommons.org/licenses/by/4.0/). Any further distribution of this work must maintain attribution to the author(s) and the title of the work, journal citation and DOI.

<sup>6</sup> Here we define symmetric radio relics as the system where the two normal vectors to the radio relics agree and are consistent with the hypothesized merger axis.

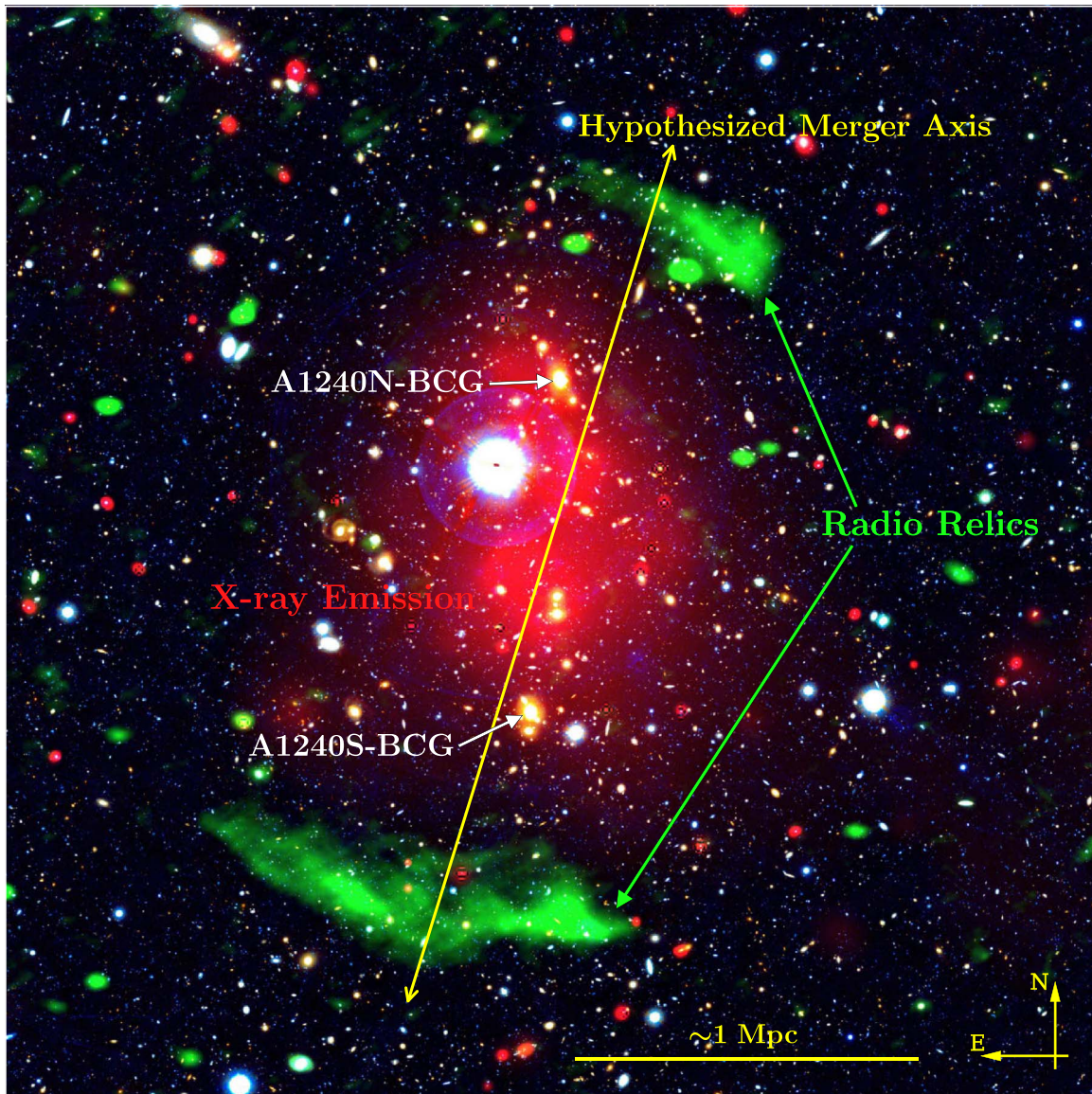


**Figure 1.** LOFAR, Subaru, and Chandra view of the merging cluster A1240. The composite image shows the  $16'.5 \times 16'.5$  ( $3.2 \text{ Mpc} \times 3.2 \text{ Mpc}$ ) region centered on A1240. The intensity in green represents the 143 MHz radio emission measured with LOFAR (Hoang et al. 2018). The intensity in red represents the 52 ks Chandra X-ray surface brightness map. The background RGB image is created using the Subaru/Suprime-Cam  $r$ ,  $r + g$ , and  $g$  filter data for the red, green, and blue channels, respectively. The hypothesized merger axis is aligned with the X-ray elongation and also perpendicular to both radio relics.

Mach numbers of  $\sim 3$  were derived. Bonafede et al. (2009) also found that the mean level of fractional polarization in the relics is high ( $\sim 30\%$ ), reaching up to  $70\%$ ; in general, a smaller angle between the merger axis and the plane of the sky is believed to produce a larger polarization fraction. Hoang et al. (2018) used high-resolution and wide-frequency range (LOFAR 143 MHz, GMRT 612 MHz, and VLA 3 GHz) observations and found that the spectral indices of both relics steepen from the outer edges toward the cluster center. Hoang et al. (2018) revealed that the projected largest linear size and radio power of the southern relic are twice as large and three times higher than those of the northern relic, respectively. From the measurement of the mean fractional polarization, they estimated the viewing angle<sup>7</sup> to be  $\alpha \lesssim 51^\circ$ .

<sup>7</sup> In this study, the viewing angle  $\alpha$  is defined to be the angle between the merger axis and the plane of the sky. Note that the definition used by Hoang et al. (2018) is  $90^\circ - \alpha$ .

Now, to complete the merging scenario of A1240, among the most important missing data are its DM substructures and masses. The mass is critical in estimating the timescale of the merger because it determines the collision speed, which is related to the shock propagation speed and the position of the relics. As the merging system departs from the hydrostatic/dynamic equilibrium, mass estimates based on X-ray, Sunyaev–Zel’dovich (SZ), or galaxy-velocity observations are expected to produce biased results. To address the issue, we perform a weak-lensing (WL) analysis with Subaru/Suprime-Cam imaging data. No measurement of the WL signal has been reported to date for the A1240 field. Our WL study of A1240 and its subclusters provides independent mass estimates. Although WL mass estimates are not totally bias-free, the method is least affected by the dynamical state of the system.

In addition to WL, we investigate the cluster galaxy position/velocity distribution of A1240 with our MMT/Hectospec data. Barrera et al. (2009, hereafter B09) used the

TNG-DOLORES/MOS and Sloan Digital Sky Survey (SDSS) DR7 data and identified the north–south bimodal structure with 62 cluster members in A1240. Furthermore, 27 members were assigned to its companion cluster, A1237. B09 estimated the line-of-sight (LOS) velocity difference between the two substructures to be  $\sim 400 \text{ km s}^{-1}$ . Golovich et al. (2019a, 2019b) increased the total number of spectroscopic members of A1240 to 146 using Keck/DEIMOS observations, confirming both the bimodality and LOS velocity reported by B09. G19b also identified 24 member galaxies for A1237. Our MMT/Hectospec observation brings the total number of confirmed members to  $\sim 432$  in the A1240 field (A1240+A1237), which is a significant (a factor of 2.5) increase. Aided by our Subaru imaging data, we refine our understanding of the cluster substructure and dynamical state. Using the SDSS spectroscopic catalog of galaxies, we also explore the surrounding structures of A1240 out to a clustercentric radius of  $\sim 100 \text{ Mpc}$ . Finally, combining our multiwavelength observations from radio to X-ray with Monte Carlo analysis, we constrain the merging scenario of A1240.

Throughout the paper, we adopt a flat  $\Lambda$ CDM cosmology with  $H_0 = 70 \text{ km s}^{-1} \text{ Mpc}^{-1}$ ,  $\Omega_M = 0.3$ , and  $\Omega_\Lambda = 0.7$ . At the redshift of A1240,  $z = 0.195$ , an angular scale of  $1''$  corresponds to a physical scale of  $\sim 3.24 \text{ kpc}$  ( $\sim 194 \text{ kpc arcmin}^{-1}$ ). Unless otherwise specified, north is up and east is left in our two-dimensional (2D) image presentations. All magnitudes are in the AB magnitude system. The  $M_{200}$  ( $M_{500}$ ) value refers to a halo mass within a spherical volume of radius  $r_{200}$  ( $r_{500}$ ), at which the mean cluster density is 200 (500) times the critical density of the universe at the redshift of the cluster.

We structure our paper as follows. Section 2 describes our data and reduction methods. We present our analysis of the cluster member distributions and WL signal in Section 3. Our results are compared with previous studies and we present a new merging scenario in Section 4 before we conclude in Section 5.

## 2. Observations

### 2.1. Subaru/Suprime-Cam

The A1240 field was observed with the Subaru Prime Focus Camera (Suprime-Cam; Miyazaki et al. 2002) on 2014 February 25 in the  $g$  and  $r$  bands (PI: D. Wittman) with total integrations of 720 and 2880 s, respectively, as part of the MC<sup>2</sup> radio-relic-selected optical imaging survey (Golovich et al. 2019a). We used dithering and field rotation among four and eight pointings for  $g$  and  $r$ , respectively. This not only reduces the effects of cosmic rays but also azimuthally distributes the saturation trails and diffraction patterns from bright stars, which are removed in the later stacking process. The reliability of this scheme for detecting faint, small galaxies near bright stars has been demonstrated in a series of our Subaru/Suprime-Cam WL studies (e.g., Jee et al. 2015, 2016; Finner et al. 2017, 2021).

We used the SDFRED2 package<sup>8</sup> (Ouchi et al. 2004) for low-level data reduction steps such as overscan and bias subtraction, flat-fielding, geometric distortion correction, atmospheric dispersion correction, autoguider shade masking, etc. We obtained astrometric solutions for individual frames using SExtractor<sup>9</sup> (Bertin & Arnouts 1996) and SCAMP<sup>10</sup> (Bertin 2006) with SDSS DR9 as a reference. To create the

final mosaic images, we performed a two-step process of median-stacking and weighted-averaging coaddition for each filter with the SWarp software<sup>11</sup> (Bertin et al. 2002). See our previous MC<sup>2</sup> studies (e.g., Jee et al. 2015, 2016; Finner et al. 2017) for details about Suprime-Cam data reduction procedures.

For both  $g$ - and  $r$ -band mosaic images, we performed object detection and photometry with SExtractor in dual-image mode. We used the deeper  $r$ -band image and its associated output weight map from SWarp for object detection. The dual mode ensures that the same object positions and apertures are used for the photometry in different filter sets. We identified objects with an area of at least five connected pixels above twice the local background rms. Separation of blended objects was performed using `DEBLEND_NTHRESH = 64` and `DEBLEND_MINCONT = 10-4`. For the photometric measurements, we used the rms maps, which were constructed from the SWarp-produced weight maps.

Since the Subaru/Suprime-Cam filter throughputs are similar to those of SDSS, we calibrated the Subaru photometry using the star catalog from SDSS DR16, which covers the A1240 field. Since the SDSS magnitudes were corrected for Galactic extinction (Schlafly & Finkbeiner 2011), our calibration also includes the correction. We employed `MAG_AUTO` to estimate the total flux for each object. For the color estimation, we used the magnitude measured within the isophotal area (`MAG_ISO`). The limiting magnitudes where the detection completeness fraction reaches 50% (Harris 1990) are 26.2 and 27.0 mag in `MAG_AUTO` for the  $g$  and  $r$  filters, respectively.

### 2.2. MMT/Hectospec

Spectroscopic observations (PI: K. Finner) of the A1240 field were carried out with the 6.5 m MMT/Hectospec as part of the Korean GMT (K-GMT) project. The 300 fiber Hectospec (Fabricant et al. 2005) instrument was configured for two pointings utilizing the  $270 \text{ groove mm}^{-1}$  grating with a spectral coverage of 3650–9200 Å. Cluster member candidates within the  $1^\circ$  field of view of the instrument were selected from Subaru imaging, archival SDSS imaging, and SDSS photometric redshifts. For the Subaru and SDSS imaging, candidates were selected within  $\Delta(g-r) \pm 0.1$  of a linear fit to the existing spectroscopic redshifts in a  $g-r$  versus  $r$  color-magnitude diagram (CMD). Photometric redshift candidates were selected within  $z = 0.195 \pm 0.05$ . The candidates were split into a bright configuration with objects  $r \leq 20$  and a faint configuration with  $r \leq 21$ . The bright configuration was observed on 2019 March 5 for 1 hr of integration, and the faint configuration was observed on 2019 March 26 with 2 hr of integration, both on a 20 minute cadence.

We reduced the MMT/Hectospec observations with the HSRED v2.1 pipeline<sup>12</sup> provided by the Telescope Data Center (TDC) at SAO, originally written by Richard Cool. The krypton lamp light, one of the MMT PenRay emission calibration lamps, has affected part of the observations as emission or absorption and makes it difficult to estimate redshifts correctly. For this observation, we used the TDC-reduced data. We derived redshifts for each of 477 spectra through a cross-correlation routine with a set of template spectra using the RVSAO add-on package in IRAF (Kurtz & Mink 1998).

<sup>8</sup> <https://naoj.org/Observing/Instruments/SCam/sdfred/sdfred2.html.en>

<sup>9</sup> <https://www.astromatic.net/software/sextactor>

<sup>10</sup> <http://www.astromatic.net/software/scamp>

<sup>11</sup> <http://www.astromatic.net/software/swarp>

<sup>12</sup> <https://github.com/MMTObservatory/hsred>

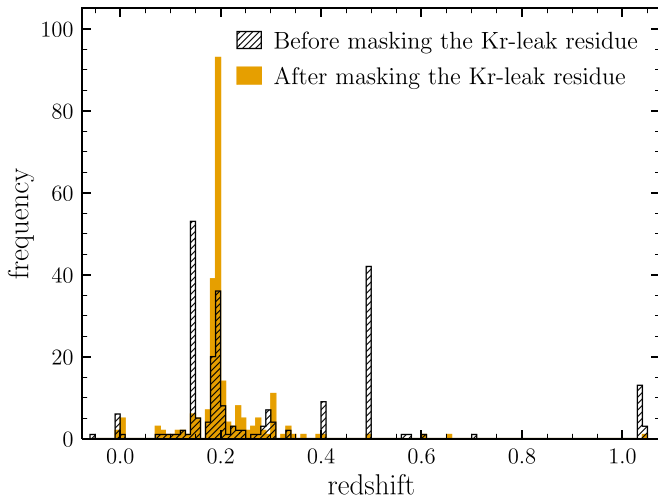


**Figure 2.** Redshift distribution from the first-night MMT observation, which was affected by the krypton lamp light. The hatched histogram is obtained from the redshift estimates before the calibration lamp light leak residuals were masked out. The orange histogram is the result when we masked out the residuals. The number of cluster member candidates in the first-night observation increased from 64 ( $\sim 27\%$ ) to 149 ( $\sim 62\%$ ) after the correction for the light leaks was performed.

Figure 2 shows the effect of the krypton light leak on the redshift measurements. Because some residue from the krypton light leak is still evident in the TDC-cleaned spectra (hatched histogram), we provided a list of masked regions for the residual to estimate redshifts more reliably (orange histogram). After the residuals are masked out, the number of A1240 cluster galaxy candidates increases from 64 ( $\sim 27\%$ ) to 149 ( $\sim 62\%$ ) in the bright configuration.

We adopted a cross-correlation score  $r$ -value (Tonry & Davis 1979)  $R_{XC}$ , a measure of the significance of the cross-correlation peak, greater than 4 as secure redshift measurements. When we used the criteria of  $R_{XC} > 4$  and  $z_{\text{err}} < 0.001$  ( $v_{\text{err}} < 300 \text{ km s}^{-1}$ ), we obtained 443 reliable redshift measurements from our new MMT observations, including 236 member candidates. In the following section, we describe the details of the membership determination.

### 3. Analysis

#### 3.1. Cluster Galaxy Distributions

##### 3.1.1. Membership Determination

To maximize the number of spectroscopically confirmed cluster galaxies, we collected publicly available spectroscopic redshifts in the A1240 field. B09 provided redshifts of 145 galaxies. They combined 118 redshifts acquired at the TNG telescope and 32 publicly available SDSS galaxies (five galaxies are in common). As part of the MC<sup>2</sup> radio-relic-selected spectroscopic survey (Golovich et al. 2019a), we observed A1240 with the DEIMOS multiobject spectrograph with the Keck II telescope on 2013 December 3 and 2015 February 16 (PI: W. Dawson). The spectroscopic observations were conducted with two slit masks for the SDSS-targeted galaxies. We obtained 188 spectroscopic redshifts of galaxies. In addition, from SDSS DR16, we retrieved 168 spectroscopic galaxies within  $R = 25'$  of the position at R.A. =  $11^{\text{h}}23^{\text{m}}36^{\text{s}}.0$ , decl. =  $+43^{\circ}05'04''.2$ . We found that there are 37 galaxies in common among the different catalogs and compiled a total of 464 published redshifts.

We combined these spectroscopic redshifts from the literature and our MMT measurements in the A1240 field and created a final catalog of 934 galaxies. Out of the 464 published spectroscopic redshifts, seven galaxies are also present in our MMT/Hectospec catalog, and their values agree well up to the fourth decimal place ( $\Delta z = 0.000191$ ;  $\Delta v = 57.2 \text{ km s}^{-1}$ ). We used our MMT redshift measurements and recently published spectroscopic redshifts for duplicated targets. The distributions of galaxies in the combined spectroscopic catalog as a function of redshift are displayed in the top panel of Figure 3. Table 1 lists the redshift information of the final catalog.

To separate cluster member candidates from foreground and background objects, we performed iterative  $3\sigma$  clipping, estimating the mean redshift and velocity dispersion using the biweight estimator (Beers et al. 1990). In combination with the publicly available data, we obtained 432 member (candidate) galaxies in the A1240 field (stacked histograms in the bottom panel of Figure 3) out of 898 reliable redshift measurements.<sup>13</sup>

#### 3.1.2. Galaxy Number and Luminosity Distributions

Although we tripled the number of A1240 spectroscopic members, the spectroscopic catalog is still far from complete. Thus, we used the photometric catalog from Subaru/Suprime-Cam to augment our spec- $z$  member catalog and create the final cluster galaxy catalog. Since the  $g-r$  color brackets the redshifted 4000 Å break—the characteristic spectral feature caused by the dominant old, cool stellar populations—at  $z = 0.195$ , its red sequence is readily distinguished in the CMD. Figure 4 shows the  $g-r$  versus  $r$  CMD of the A1240 field. The locus of the red sequence is well defined photometrically and also nicely traced by the spectroscopically confirmed members. The color–magnitude relation of the red sequence is determined from the best-fit linear regression of the spectroscopic members within the  $g-r$  color range of  $1.079 \pm 0.187$ , which is computed with the biweight estimator. The resulting best-fit result is  $g-r = -0.032r + 1.723$ . This relation is used for identifying photometric red-sequence galaxies. We restricted the length of the red sequence to objects 6 mag fainter than the brightest cluster galaxy (BCG)<sup>14</sup> and width to  $\pm 1\sigma$ , where  $\sigma$  is a robust standard deviation of the  $g-r$  colors of the confirmed member galaxies.

In addition to the above selection criteria in the color–magnitude space, we employed the size–magnitude relation in eliminating stars from the photometric red-sequence catalog. Figure 5 shows the half-light radius (FLUX\_RADIUS) versus  $r$  (MAG\_ISO) relation for the same objects in Figure 4. The pointlike sources and bright saturated stars are either more compact or brighter than the confirmed member galaxies. We merged the resulting red-sequence catalog and the spectroscopic cluster galaxy catalog to investigate the projected surface density distributions of the cluster galaxies described below.

Figure 6 shows the cluster galaxy distributions in the central  $27' \times 27'$  ( $5.24 \text{ Mpc} \times 5.24 \text{ Mpc}$ ) region of the A1240 field. In panel (a), we display the color-composite image created from Subaru/Suprime-Cam  $r$ -,  $g+r$ -, and  $g$ -band data. We mark the positions of the BCGs in A1240 and A1237. We refer to two BCGs of A1240 as A1240N-BCG and A1240S-BCG, which

<sup>13</sup> The criteria are  $R_{XC} > 4$  and  $v_{\text{err}} < 300 \text{ km s}^{-1}$ .

<sup>14</sup> Following our previous MC<sup>2</sup> work (G19b), we determined the width of the red-sequence box to be 6 mag, sufficient to cover the magnitude range of the spectroscopically confirmed member galaxies.

are located at the approximate centers of the northern (A1240N) and southern (A1240S) subclusters in A1240. Our current data do not show distinct substructures in A1237. The two BCGs in A1237 are labeled as A1237BCG-N and A1237BCG-S according to their location in the Subaru image. In panel (b), we display both spectroscopic (circles) and photometric (gray dots) members. We color-coded the spectroscopic member galaxies using the relative velocity difference with respect to the rest-frame central velocity of A1240.

To detect density peaks and substructures, we adaptively smoothed the 2D density distribution of cluster galaxies. The surface number density map was produced by applying the CIAO<sup>15</sup> (Fruscione et al. 2006) `csmooth` tool with a minimal smoothing scale of  $1'$  ( $\approx 0.194$  Mpc at  $z=0.195$ ) and a significance between  $3\sigma$  and  $5\sigma$ . The resulting map is displayed in panel (c). Panel (d) shows the adaptively smoothed density map weighted by luminosity (SExtractor isophotal flux `FLUX_ISO` parameter). Here we reused the kernel size map output by `csmooth` during the creation of the number density map.

Both the number and luminosity-weighted density maps clearly identify three overdense regions aligned in the north–south direction. A1240 consists of two subclusters (A1240N and A1240S) separated by  $\sim 1$  Mpc. This bimodality is consistent with the findings of B09 and G19b. About  $\sim 1.6$  Mpc to the south of A1240S is A1237, which is also shown in B09 and G19b.

Figure 7 shows the redshift distribution of the cluster galaxies belonging to each substructure. Because of the small differences in the LOS velocities and the overlapping virial radii, it is difficult to assign a unique membership to each galaxy. Thus, we relied on the projected separation from the substructure center to determine the substructure membership, labeling an object as a member if it is within  $\sim 2.5$  (half of the distance between A1240N and A1240S, i.e.,  $\sim 0.48$  Mpc). To define the substructure center, we used the luminosity-weighted density map. We note that similar results are obtained when the number density map is used instead. The resulting numbers of objects are 45, 51, and 19 for A1240N, A1240S, and A1237.

The LOS velocity difference between A1240N and A1240S is estimated to be smaller ( $83 \pm 185$  km s<sup>-1</sup>) than our previous estimate ( $394 \pm 117$  km s<sup>-1</sup>) from G19b. With respect to A1240S, A1237 is offset by  $295 \pm 219$  km s<sup>-1</sup>, which is in agreement with the estimates of B09 ( $59 \pm 203$  km s<sup>-1</sup>) and G19b ( $88 \pm 159$  km s<sup>-1</sup>) within the errors. Therefore, our analysis suggests that the LOS velocity difference among the three substructures is consistent with zero.

Velocity dispersions are computed with the biweight estimator. We find  $909 \pm 116$ ,  $841 \pm 109$ , and  $613 \pm 87$  km s<sup>-1</sup> for A1240N, A1240S, and A1237, respectively. Based on GMM analysis (including more member galaxies), G19b quoted  $706 \pm 52$  and  $727 \pm 68$  km s<sup>-1</sup> for A1240N and A1240S, respectively, which are broadly consistent with the current estimates. Our velocity dispersion for A1237 is also consistent with the B09 estimate ( $738_{-54}^{+82}$  km s<sup>-1</sup>). Detailed discussions on the comparison with the previous studies are presented in Section 4. For each subcluster, the 2D density peak coordinates, redshift and velocity dispersion measurements, and bootstrapped uncertainties are summarized in Table 2. Note that sometimes an incorrect value of  $z = 0.159$  is quoted for the redshift of A1240 in

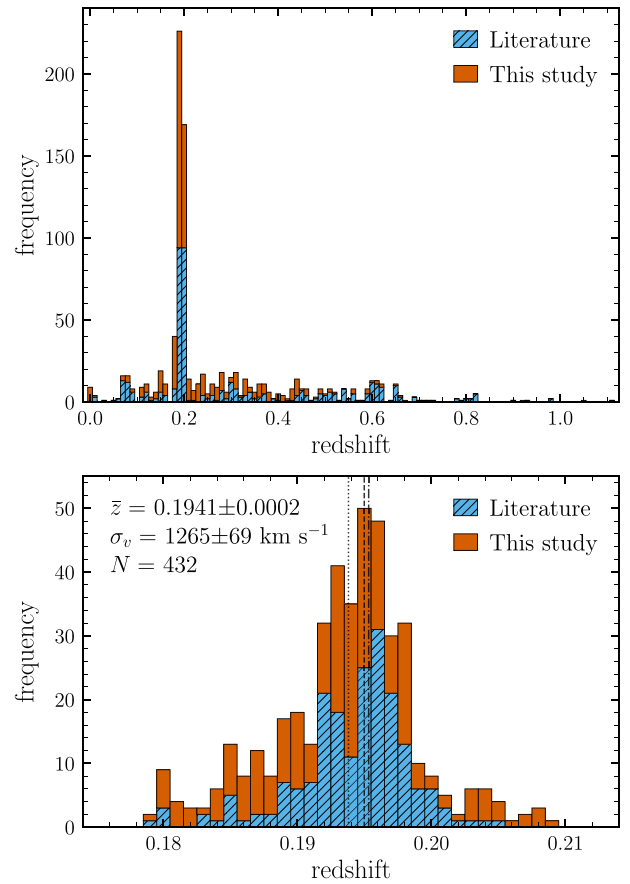


**Figure 3.** Redshift distributions for our combined spectroscopic catalog in the A1240 field. The blue hatched bars represent the redshift distribution of galaxies from the literature, including SDSS DR16 galaxies, while the orange filled stacked bars are from our MMT/Hectospec observations. Duplicates are removed. The top panel shows all galaxies with spectroscopic redshifts listed in Table 1. The redshift distribution of the member (candidate) galaxies is illustrated in the bottom panel. Spectroscopically confirmed members are determined by performing an iterative  $3\sigma$  clipping process with the biweight estimator. The total number of member candidates is 432, with a global (biweight) mean redshift of  $0.1941 \pm 0.0002$  and a rest-frame velocity dispersion of  $1265 \pm 69$  km s<sup>-1</sup>, along with  $1\sigma$  uncertainties derived from 10,000 bootstrap resamplings. Bins have widths of  $\Delta z = 0.01$  (top) and  $\Delta z = 0.001$  (bottom). The dotted–dashed and dashed vertical lines demonstrate the robust mean redshifts of the northern and southern luminosity subclumps of A1240, whereas the dotted vertical line shows that of the A1237 luminosity clump (see Figure 7).

the literature (e.g., Kempner & Sarazin 2001; Bonafede et al. 2009; Ferretti et al. 2012; de Gasperin et al. 2014; van Weeren et al. 2019; Wittor et al. 2021). In fact, the value  $z = 0.159$  was estimated from the apparent magnitude of the 10th brightest galaxy in A1240 (David et al. 1999).

### 3.1.3. Filamentary Structure around A1240

Numerical simulations have shown that galaxy clusters grow by accreting galaxies, groups, or clusters along their host filaments. Therefore, one of the natural expectations is that cluster merger axes might preferentially align with the orientations of the filaments. Our galaxy analysis with Subaru and MMT data shows that the three substructures in the A1240 field form an  $\sim 4$  Mpc filamentary structure in the north–south orientation. Here we investigate the surrounding environments of A1240 out to radii of  $\sim 100$  Mpc from the cluster center and report a discovery of a much larger scale ( $\sim 80$  Mpc)

<sup>15</sup> <https://cxc.harvard.edu/ciao4.13/>

**Table 1**  
Spectroscopic Redshift Catalog of the A1240 Field

R.A. (J2000) (deg) (1)	Decl. (J2000) (deg) (2)	$cz$ ( $\text{km s}^{-1}$ ) (3)	$z$ (4)	$z_{\text{err}}$ (5)	$R_{\text{XC}}$ (6)	Catalog Source (7)
170.2139000	42.9799575	$80,183 \pm 82$	0.267460	$2.72518 \times 10^{-4}$	3.1	MMT
170.2442542	43.2169419	$68,205 \pm 33$	0.227509	$1.10282 \times 10^{-4}$	12.3	MMT
170.2460167	43.1449014	$34,216 \pm 72$	0.114131	$2.38641 \times 10^{-4}$	3.9	MMT
170.2488167	43.2495383	$66,035 \pm 11$	0.220270	$3.80040 \times 10^{-5}$	11.7	MMT
170.2498042	42.8980903	$131,726 \pm 22$	0.439392	$7.40362 \times 10^{-5}$	11.3	MMT
170.2548250	43.1294517	$98,990 \pm 13$	0.330195	$4.22305 \times 10^{-5}$	11.6	MMT
170.2631375	42.9662894	$58,725 \pm 42$	0.195887	$1.40097 \times 10^{-4}$	7.6	MMT
170.2673167	43.0931739	$132,779 \pm 28$	0.442902	$9.38973 \times 10^{-5}$	8.5	MMT
170.2721083	42.8627586	$59,767 \pm 53$	0.199360	$1.75617 \times 10^{-4}$	7.9	MMT
170.2747250	43.2392617	$54,690 \pm 21$	0.182426	$6.94714 \times 10^{-5}$	19.1	MMT

**Note.** Table 1 is published in its entirety in machine-readable format. A portion is shown here for guidance regarding its form and content. The columns are as follows: (1) R.A. and (2) decl. in degrees (J2000.0), (3) redshift velocity and measurement uncertainty in kilometers per second, (4) redshift and (5) uncertainty, and (6) cross-correlation  $r$ -value obtained from RVSAO (valid only for the MMT catalog). Column (7) gives the references for the spectroscopic data. The codes MMT, B09, G19, and SDSS refer our MMT/Hectospec observations, B09, Golovich et al. (2019a), and SDSS DR16.

(This table is available in its entirety in machine-readable form.)

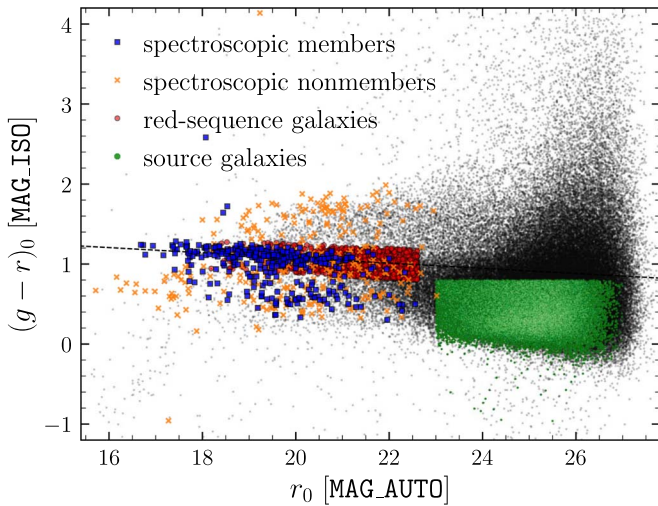


**Figure 4.** The CMD of the photometric and spectroscopic catalogs of the A1240 field. Black scatters show the Subaru photometric catalog. Blue squares represent galaxies spectroscopically confirmed as members of A1240 and A1237 (bottom panel of Figure 3), while orange crosses indicate foreground-plus-background galaxies. The locus of red-sequence galaxies is well defined with confirmed member galaxies. We applied its color–magnitude relation (dashed line) to identify red-sequence member candidates (red points) from the photometric catalog. The source galaxies selected for the WL analysis are shown as a green Hess diagram with square-root scaling (see Section 3.2.4 for details).

filamentary structure whose orientation is remarkably consistent with the hypothesized merger axis of A1240.

We retrieved a galaxy catalog for the radius of  $R < 9^\circ$  ( $\sim 100$  Mpc at  $z = 0.195$ ) region centered on A1240 from the SDSS DR16 archive. In addition, we compiled a list of galaxy clusters at  $R < 0.9^\circ$  ( $\sim 10$  Mpc) whose redshifts are similar to that of A1240 from the literature (Abell 1958; Abell et al. 1989; Koester et al. 2007; Hao et al. 2010; Wen et al. 2012; Wen & Han 2015).<sup>16</sup> The result is displayed in Figure 8. Remarkably,

<sup>16</sup> For example, a group of galaxies  $\sim 1.9$  Mpc north of A1240 was identified as a cluster by Hao et al. (2010; GMBCG170.89) and Wen et al. (2012; WHL J112333.6+431447). Another example is WHL J112352.7+424542 (Wen et al. 2012), detected  $\sim 2.3$  Mpc to the southeast of A1237. These two clusters are marked with yellow stars in the right panel of Figure 8.

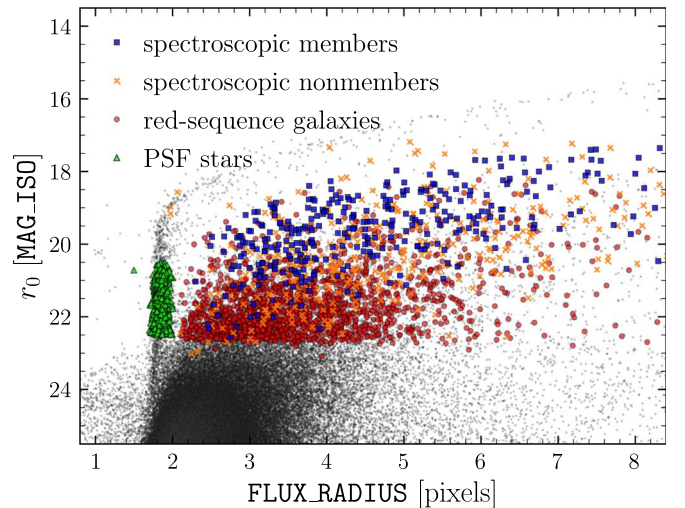


**Figure 5.** Size–magnitude diagram for the photometric and spectroscopic catalogs of the A1240 field. The stars follow a tight locus around a half-light radius (FLUX\_RADIUS from SExtractor) of 1.8 pixels. The pointlike objects, even saturated brighter stars, are clearly distinguished from the spectroscopically confirmed members (blue squares). The stellar size–magnitude relations are used for separating stars and photometric red-sequence galaxies, along with the color–magnitude relation in Figure 4. The green triangles indicate stars selected for the PSF modeling in Section 3.2.2.

we find that A1240 is embedded within a much larger filament stretched out to  $\sim 80$  Mpc whose orientation is in good agreement with the hypothesized merger axis. Also, the six known (candidate) clusters, together with the three substructures within the Subaru field, form a  $\sim 20$  Mpc-long filament in the same north–south orientation. The relative rest-frame LOS velocities  $|\Delta v_{\text{rf}}|$  of these clusters are less than  $\sim 300 \text{ km s}^{-1}$ , except for the southernmost A1253 with  $\Delta v_{\text{rf}} \sim 1100 \text{ km s}^{-1}$ . Moreover, the northern and southern ends of the  $\sim 80$  Mpc-long filament do not differ greatly in their LOS velocities. These facts suggest that the filament around A1240 may be nearly aligned with the plane of the sky. It will be interesting to investigate the cosmic filament detected in the current study with WL based on future wider and deeper imaging data.

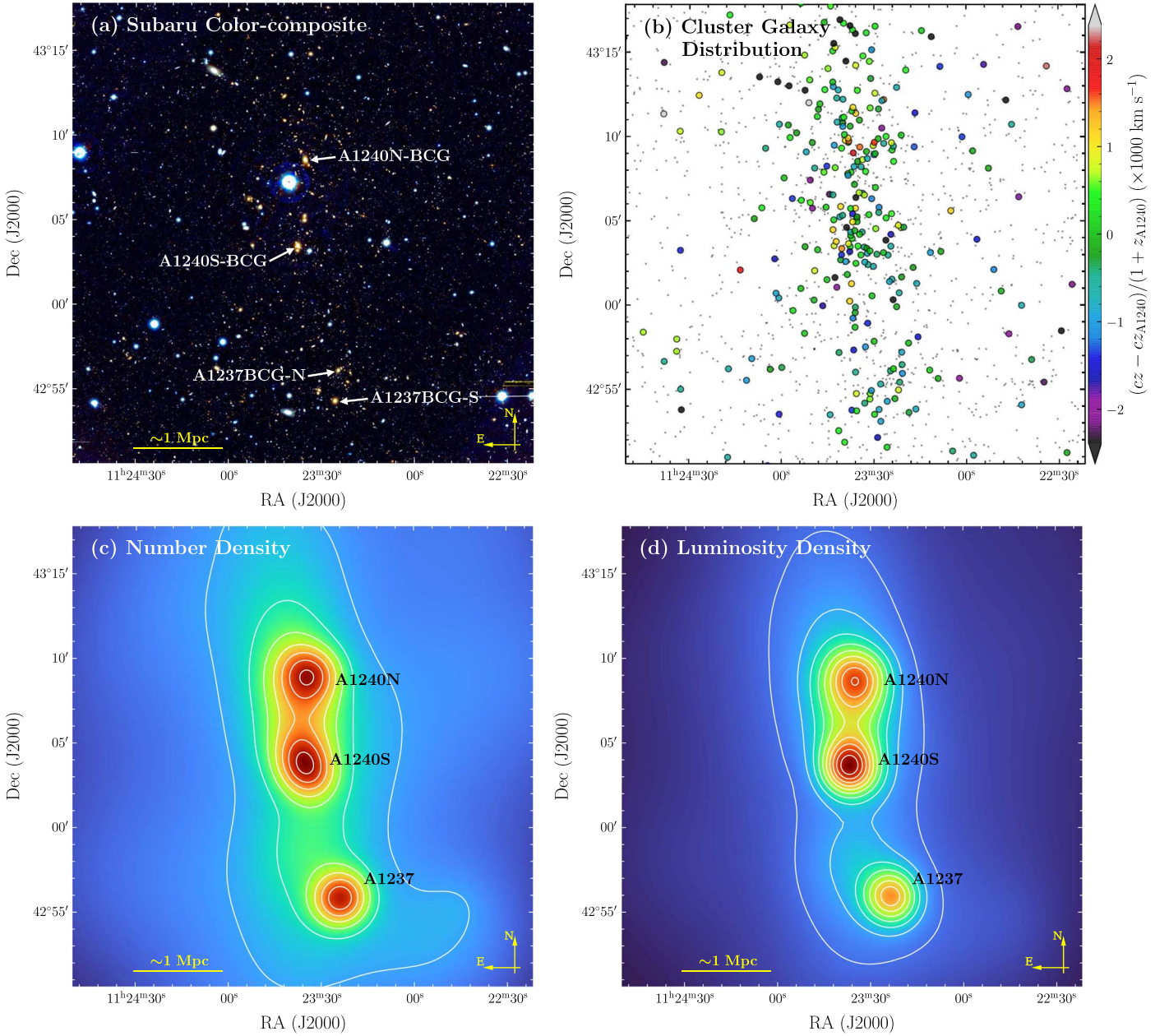


**Figure 6.** The A1240 optical image and cluster member distribution. (a) Color-composite image of the central  $27' \times 27'$  ( $5.24 \text{ Mpc} \times 5.24 \text{ Mpc}$ ) region. The Subaru/Suprime-Cam  $r$ -,  $g+r$ -, and  $g$ -band data are used for the RGB channels of the image. (b) Distribution of the A1240+A1237 member (candidate) galaxies. Filled circles show the locations of the spectroscopically confirmed cluster members, color-coded with the relative velocity difference with respect to the cluster mean velocity of A1240. Gray dots are the photometrically selected (red-sequence) members. (c) Adaptively smoothed galaxy number density map. We used the CIAO `csmooth` tool with a minimum (maximum) significance of  $3\sigma$  ( $5\sigma$ ). The resulting minimal smoothing scale is  $60''$  ( $\approx 0.194 \text{ Mpc}$  at the cluster redshift). (d) Adaptively smoothed luminosity-weighted galaxy density map. To smooth the luminosity map, we reused the kernel scale map that `csmooth` generated for the number density map. In the bottom panels, the contours begin at  $1\sigma$  above mean density and are linearly spaced in units of  $\sigma$ , where  $\sigma$  is the standard deviation of density distribution. The galaxy distribution shows that A1240 consists of two subclusters (A1240N and A1240S) separated by  $\sim 0.96 \text{ Mpc}$ . A1237,  $\sim 1.56 \text{ Mpc}$  to the south of A1240S, is detected as a compact distribution of galaxies in both luminosity and number density maps with a mean redshift similar to that of A1240.

## 3.2. Weak Lensing

### 3.2.1. Basic Theory

In this section, we provide a brief overview of WL theory and its formalism. For details, we refer the reader to review papers (e.g., Narayan & Bartelmann 1996; Bartelmann & Schneider 2001; Kneib & Natarajan 2011).

Galaxy clusters act as a gravitational lens for background galaxies. In the WL regime, where a source galaxy is much smaller than the characteristic scale of the lensing signal

variation, the coordinate transformation by gravitational lensing can be linearized. The resulting Jacobian matrix  $\mathbf{A}$  transforming the source plane position  $\mathbf{x}$  to the image plane position  $\mathbf{x}'$  via  $\mathbf{x}' = \mathbf{A}\mathbf{x}$  is then described by

$$\mathbf{A} = (1 - \kappa) \begin{pmatrix} 1 - g_1 & -g_2 \\ -g_2 & 1 + g_1 \end{pmatrix}, \quad (1)$$

where  $\kappa$  is the convergence and  $g_{1(2)}$  is the first (second) component of the reduced shear  $g$ :

**Table 2**  
Measured Properties of Subclusters in the A1240 Field

Subcluster	Number Density Peak R.A., Decl. (deg)	Luminosity Density Peak R.A., Decl. (deg)	$z$	$\sigma_v$ (km s <sup>-1</sup> )	$\sigma_{v,SIS}$ (km s <sup>-1</sup> )	$M_{200}$ (10 <sup>14</sup> M <sub>⊙</sub> )
(1)	(2)	(3)	(4)	(5)	(6)	(7)
A1240N	170.894181, 43.148796	170.896484, 43.143749	0.195317 ± 0.000554	909 ± 116	540 <sup>+50</sup> <sub>-55</sub>	2.61 <sup>+0.51</sup> <sub>-0.60</sub>
A1240S	170.896442, 43.062998	170.903349, 43.061313	0.194987 ± 0.000486	841 ± 109	464 <sup>+55</sup> <sub>-63</sub>	1.09 <sup>+0.34</sup> <sub>-0.43</sub>
A1237	170.850419, 42.930099	170.848120, 42.933463	0.193810 ± 0.000725	613 ± 87	447 <sup>+59</sup> <sub>-68</sub>	1.78 <sup>+0.44</sup> <sub>-0.55</sub>

**Note.** The columns are as follows: (1) subcluster component, (2) and (3) coordinate of the number and luminosity-weighted density peaks (see bottom panels of Figure 6), (4) and (5) mean redshift and velocity dispersion of the luminosity peaks (see Figure 7), (6) velocity dispersion determined from the best-fit SIS profile (see Section 4.1.1), and (7) WL mass estimate based on the best-fit NFW profile (see Section 3.2.6).

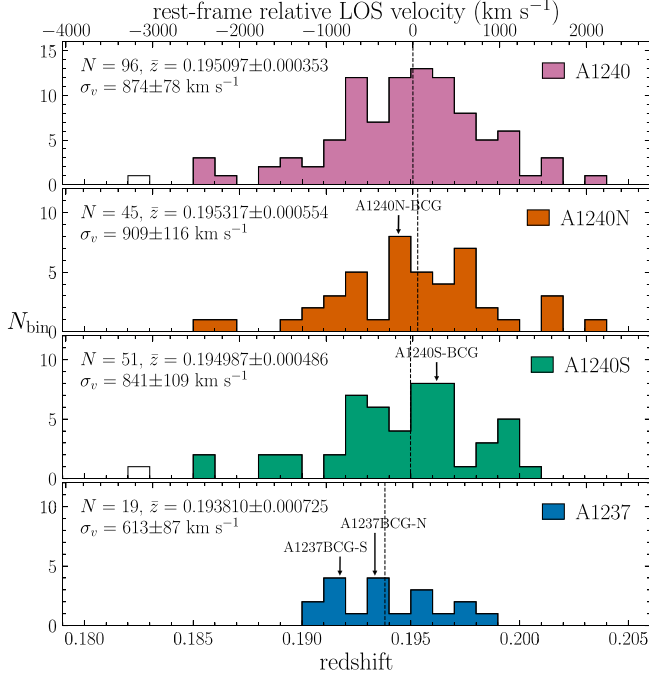


**Figure 7.** Redshift distributions of luminosity peaks. The top panel shows the combination of A1240N and A1240S, while the lower panels are redshift distributions of galaxies belonging to individual luminosity peaks within a radius of  $\sim 2.5$  ( $\sim 0.48$  Mpc). The biweight estimators are applied to measure mean redshifts (dashed vertical lines) and rest-frame velocity dispersions with measurement uncertainties extracted from the bootstrap resampling. The open histograms represent the galaxies excluded from the biweight statistics presented here. The arrows denote the spectroscopic redshifts of BCGs. The velocity scale on the top axis is centered on the A1240 rest-frame central velocity of  $z = 0.195097$  from the top panel.

$$g = (g_1^2 + g_2^2)^{1/2} \equiv \gamma / (1 - \kappa). \quad (2)$$

In Equation (2),  $\gamma$  is the shear, which approaches  $g$  when  $\kappa \ll 1$ . The convergence  $\kappa$  is the dimensionless surface mass density, defined as the ratio of the projected surface mass density  $\Sigma$  and the critical surface mass density  $\Sigma_c$ :

$$\kappa = \frac{\Sigma}{\Sigma_c}. \quad (3)$$

The critical surface density  $\Sigma_c$  is defined by

$$\Sigma_c = \frac{c^2}{4\pi G} \frac{D_s}{D_l D_{ls}}, \quad (4)$$

where  $c$  is the speed of light,  $G$  is the gravitational constant, and  $D_l$ ,  $D_{ls}$ , and  $D_s$  are the angular diameter distances from the

observer to the lens, from the lens to the source, and from the observer to the source, respectively.

The matrix  $A$  in Equation (1) transforms a circular source into an ellipse. To define the ellipticity, we model an object with an elliptical Gaussian whose semimajor and semiminor axes are  $a$  and  $b$ , respectively. The reduced shear  $g$  then becomes

$$g = \frac{a - b}{a + b}. \quad (5)$$

As the ellipse also has an orientation, one can conveniently represent both its magnitude and position angle using the complex notation

$$\mathbf{g} = g_1 + i g_2 \equiv g e^{2i\phi}, \quad (6)$$

with magnitude  $g$  in Equation (2) and orientation angle  $\phi = 0.5 \tan^{-1}(g_2/g_1)$  of the semimajor axis.

In the same manner, the unlensed (intrinsic) ellipticity of the source galaxy can be formulated as

$$\boldsymbol{\epsilon} = \epsilon_1 + i \epsilon_2. \quad (7)$$

Then, the transformation between the source galaxy intrinsic ellipticity  $\boldsymbol{\epsilon}$  and the lensed (observed) ellipticity  $\mathbf{e}$  is given by

$$\mathbf{e} = \frac{\boldsymbol{\epsilon} + \mathbf{g}}{1 + \mathbf{g}^* \boldsymbol{\epsilon}}, \quad (8)$$

where the asterisk superscript denotes the complex conjugate. In a typical WL regime where  $\kappa \ll 1$ ,  $\gamma \ll 1$ , and thus  $g \ll 1$ , in general, each galaxy's lensed ellipticity  $\mathbf{e}$  is slightly offset from its intrinsic ellipticity  $\boldsymbol{\epsilon}$ . Assuming an isotropic distribution of  $\boldsymbol{\epsilon}$ , one can obtain  $\mathbf{g}$  via

$$\mathbf{g} = \langle \mathbf{e} \rangle \quad (9)$$

when no bias is present.

### 3.2.2. PSF Modeling

In the ground-based observation, the atmospheric turbulence and instrumental imperfection cause variations in the size and ellipticity of the point-spread function (PSF). The PSF, on average, dilutes the observed shear of source galaxies, whereas locally, it induces anisotropic bias on galaxy ellipticity measurements. In order to recover the intrinsic lensing signal, it is crucial to correct for the PSF-induced dilution and anisotropy by carefully modeling the PSF. We modeled the PSF based on the principal component analysis (PCA) technique presented in Jee et al. (2007). Here we provide a

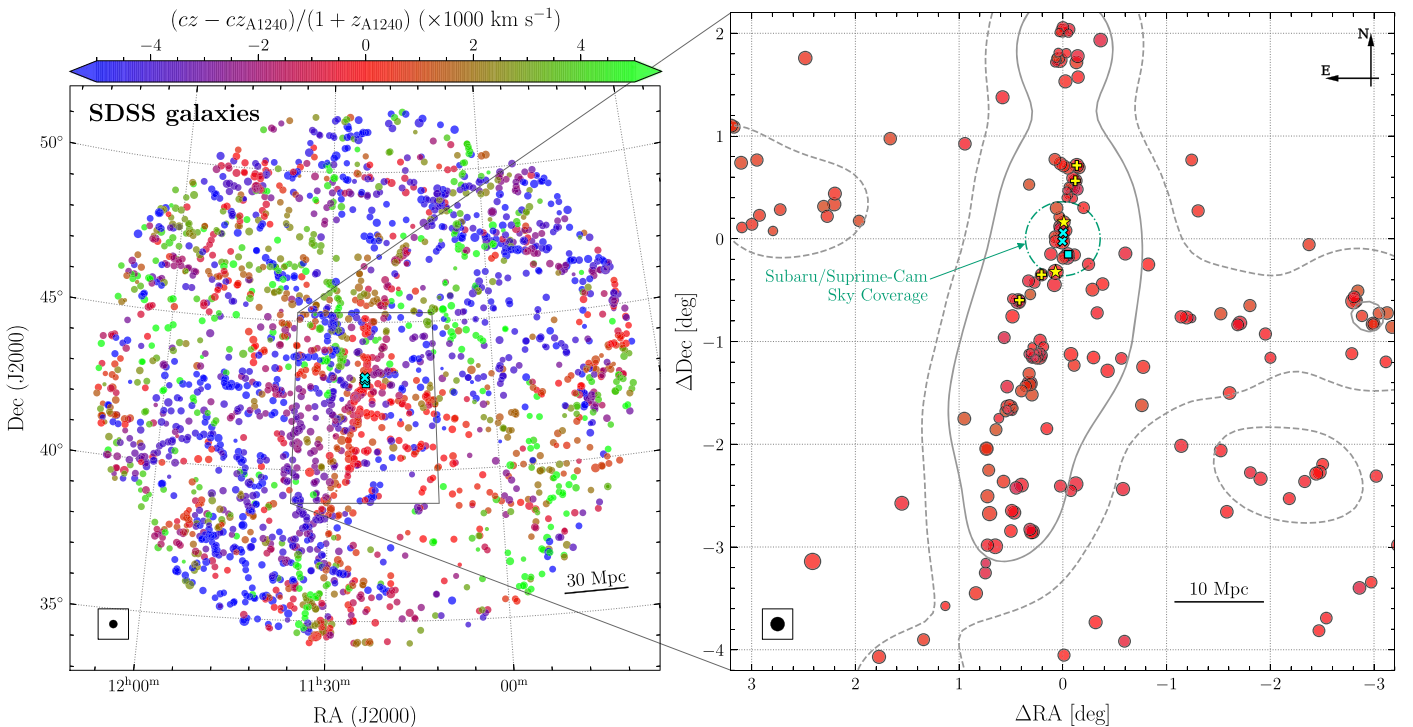


**Figure 8.** Spatial distribution of the SDSS DR16 galaxies around A1240. The left panel displays the  $\sim 3000$  objects at the clustercentric radius  $R < 9^\circ$  ( $\sim 100$  Mpc) whose rest-frame LOS velocities are within  $\pm 6000 \text{ km s}^{-1}$  of the cluster. The symbols are color-coded according to their velocities relative to the redshift of A1240. We let the symbol size scale with the dereddened SDSS  $r$ -band magnitude. The size of the black filled circle in the lower left corner box represents the A1240 BCG magnitude. A zoomed-in view of the central box is shown in the right panel, where we only show the galaxies within the velocity range  $\pm 1000 \text{ km s}^{-1}$ . The green dashed-dotted circle marks the sky coverage of the current Subaru/Suprime-Cam data. The yellow symbols indicate the positions of the (candidate) clusters of galaxies inside ( $R \lesssim 20'$ ; stars) and outside ( $20' \lesssim R \lesssim 54'$ ; plus signs) of the Subaru coverage, compiled from the literature. We created a galaxy number density map by smoothing this with an FWHM = 5 Mpc Gaussian kernel and illustrate the  $3\sigma$  and  $1\sigma$  levels above the mean number density with gray solid and dashed contours, respectively. In both panels, cyan symbols mark the locations of the luminosity density peaks of A1240 (crosses) and A1237 (square). Remarkably, A1240 is embedded within the much larger  $\sim 80$  Mpc filamentary structure elongated in the north–south orientation, which is in good agreement with the hypothesized merger axis of A1240. Also note that the six known confirmed/candidate clusters, together with the three substructures within the Subaru field, form an  $\sim 20$  Mpc filament in the same north–south orientation. The fact that both ends of the  $\sim 80$  Mpc-long filament do not differ greatly in their LOS velocities suggests that the filament may be nearly aligned with the plane of the sky.

brief overview and refer the reader to Jee et al. (2007), Jee & Tyson (2011), and Jee et al. (2013) for details.

The first step in modeling the PSF variation is to identify “good” stars from each CCD frame. We selected stars on individual resampled frames (RESAMP) produced by SWarp as a part of the two-step coadding procedure using SExtractor and the size–magnitude relations. The average number of stars per frame suitable for PSF modeling is  $\sim 30$ . We note that the density of stars in this field is lower than our previous MC<sup>2</sup> WL studies (typically containing  $\gtrsim 100$  per CCD) because of the high Galactic latitude of A1240 ( $b = 66^\circ$ ). Next, we determined the mean PSF per RESAMP and the deviations from the mean for individual stars by median-stacking the postage-stamp cutouts (21 pixels  $\times$  21 pixels) and subtracting the median from the cutouts. We performed PCA on the deviations to obtain the covariance matrix and compute the eigenvalues and corresponding eigenvectors (i.e., principal components) of the matrix. We then fitted third-order polynomials to the amplitudes along the eigenvectors to obtain a model PSF at any arbitrary position on each RESAMP. Finally, we stacked the model PSFs from the individual RESAMP images to create a coadd PSF  $P(x, y)$  at a galaxy position on the coadd image.

The left panel of Figure 9 displays the ellipticities directly measured from  $\sim 500$  stars (shown as the green triangles in the size–magnitude diagram of Figure 5) detected in the coadd frame. The stellar PSF patterns vary spatially across the entire

field. For a visual comparison, we display the ellipticities of the PSFs predicted at the same positions of the stars (middle panel). The ellipticity variation pattern of the PSFs obtained through our PCA-based model shows good agreement with that of the observed stars on the coadd frame. Some apparent outliers are attributed to cosmic-ray-affected stars, galaxies misclassified as stars, stars severely blended with nearby bright sources, or saturated trails. To examine how well the model PSFs describe the observed ellipticities quantitatively, we compare the ellipticity components before (red) and after (black) the correction in the right panel of Figure 9. The correction not only reduces the size of the scatters (compare the red and black ellipses) but also makes the centroid of the data points closer to the origin  $[(0.0022 \pm 0.0005, 0.0041 \pm 0.0005) \rightarrow (-0.0001 \pm 0.0002, -0.0003 \pm 0.0002)]$ .

### 3.2.3. Shape Measurement

Reduced shears  $g_{1(2)}$  are derived by averaging over the ellipticities of source galaxies (Equation (9)). In real observations, however, the averaged ellipticities are only biased measures of reduced shears. Sources of the systematics include model/underfitting, noise, PSF model, and pixellation biases (e.g., Bernstein 2010; Melchior & Viola 2012; Refregier et al. 2012; Mandelbaum et al. 2014). In the current study, we choose to address the issues with the “forward-modeling” and WL image simulation approaches.

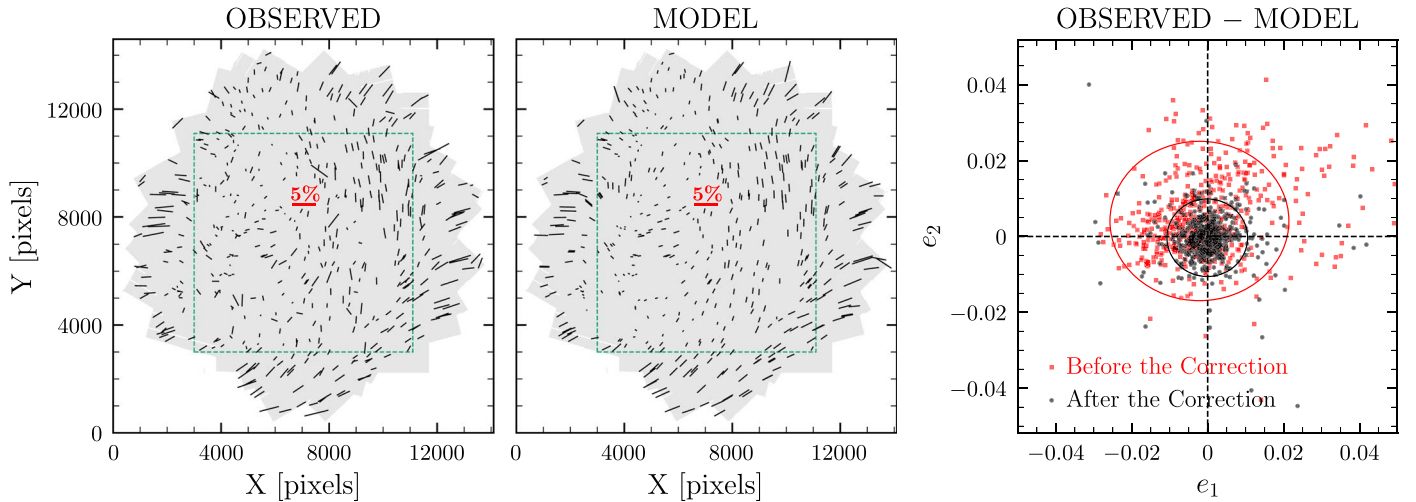


**Figure 9.** Observed vs. model PSF. The left and middle panels show the measured ellipticity distributions of observed stars and model PSFs in the Subaru  $r$ -band coadd image. The length and direction of the “whiskers” are proportional to the magnitude and orientation of the ellipticities, respectively. The corresponding model PSFs are in good agreement with the observed PSF ellipticities except for several outliers. The red sticks show the size of the 5% ellipticity. The green dashed boxes mark the central  $27' \times 27'$  region, where we performed 2D galaxy distribution mapping and WL mass reconstruction. The right panel displays the ellipticity components of the observed stars (red squares) and the residuals after applying PSF correction (black points). The ellipses, with the same color scheme, characterize the distributions of the ellipticity components. The center and radii of each ellipse are defined by the biweight locations and  $2\sigma$  in both ellipticity component axes, where  $\sigma$  is the biweight scale. The correction reduces the size of the scatters and also makes the centroid of the data points closer to the origin [(0.0022  $\pm$  0.0005, 0.0041  $\pm$  0.0005)  $\rightarrow$  (-0.0001  $\pm$  0.0002, -0.0003  $\pm$  0.0002)].

For each object detected with SExtractor, we first created a square postage-stamp cutout centered on the object ( $x_c, y_c$ ) with  $(8w + 20)$  pixels on a side, where  $w$  is SExtractor’s semimajor axis  $A\_IMAGE$  measured from the  $r$ -band mosaic image. The pixels belonging to the neighboring objects were masked out using the SExtractor segmentation map. We then convolved a 2D elliptical Gaussian function  $G(x, y)$  by a model PSF profile  $P(x, y)$  via fast Fourier transform,

$$M(x, y) = G(x, y) \otimes P(x, y), \quad (10)$$

where

$$G(x, y) = I_{bg} + I_{pk} \exp \left[ -\frac{(\Delta x \cos \theta + \Delta y \sin \theta)^2}{2\sigma_x^2} - \frac{(-\Delta x \sin \theta + \Delta y \cos \theta)^2}{2\sigma_y^2} \right], \quad (11)$$

with a background flux level  $I_{bg}$ , peak flux intensity  $I_{pk}$ ,  $\Delta x = x - x_c$ , and  $\Delta y = y - y_c$ . In Equation (11),  $\theta$  is the position angle of the semimajor axis measured from the positive  $x$ -axis in the counterclockwise direction.

To determine  $I_{pk}$ , semimajor and semiminor axes, position angle, and their uncertainties from the best-fit model (and, consequently, the ellipticity of each object), we minimized the difference between the PSF-convolved model  $M(x, y)$  and the postage-stamp galaxy image using the MPFIT code (Markwardt 2009). We let the centroid ( $x_c, y_c$ ) and the background level  $I_{bg}$  remain fixed to the SExtractor values (XWIN\_IMAGE, YWIN\_IMAGE) and BACKGROUND, respectively, throughout the fitting. The ellipticity measurement errors were calculated by propagating the uncertainties of the best-fit parameters.

The ellipticity measurement obtained above needs to be calibrated. We performed WL image simulations and determined a global multiplicative correction factor of 1.22. Readers are referred to Jee & Tyson (2011) and Jee et al. (2013) for details about the simulations. We applied the inverse-variance

weighting scheme to estimate reduced shears, considering the dispersion of the ellipticity distribution and the measurement uncertainties as follows:

$$g_{1(2)} = m_{1(2)} \frac{\sum_{i=1}^N e_{1(2)} \mu_i}{\sum_{i=1}^N \mu_i}. \quad (12)$$

In the above equation,  $\mu_i$  is the weight,

$$\mu_i = \frac{1}{\sigma_{SN}^2 + (\delta e_i)^2}; \quad (13)$$

$m_{1(2)}$  is the shear multiplicative factor;  $\sigma_{SN}$  is the shape noise ( $\sim 0.25$ ); and  $\delta e_i$  is the measurement error per ellipticity component for the  $i$ th galaxy. We found that our additive bias (typically arising from PSF model bias) is negligible.

### 3.2.4. Source Galaxy Selection and Redshift Estimation

As most lensing signals come from a faint population at high redshifts, ideally, the redshifts from large spectroscopic or multiwavelength photometric samples are needed to enable a clean separation of background sources. However, neither our current redshift nor the photometric data provide the capability. Thus, we instead use the redshift–magnitude–color relation to select source galaxies and estimate their redshifts. Although less than ideal, this method has been used in numerous studies and proven to be practically useful for identifying substructures and quantifying their masses.

We defined our source population as the objects fainter and bluer than the A1240+A1237 red sequence. The color–magnitude selection criteria are  $23 < r < 27$  and  $-1.0 < g - r < 0.8$ . The bright end is  $\sim 0.5$  mag fainter than the faintest spectroscopic cluster member to minimize the contamination by bright foreground galaxies and blue members while keeping the source density sufficiently high, whereas the faint end is approximately the limiting magnitude in  $r$ . We also required the sources to have well-defined shapes after their PSF effects are removed. Specifically, first, the elliptical Gaussian fitting

must be successful (the MPFIT STATUS parameter should be unity). Second, the ellipticity measurement error should be less than 0.3. Third, the (deconvolved) semimajor axis needs to be greater than 0.3 pixels. Finally, the ellipticity magnitude  $(e_1^2 + e_2^2)^{1/2}$  must be less than 0.9. As illustrated in Figure 14 of Jee et al. (2013), sources failing to meet these requirements usually form a characteristic pattern in the  $e_1$  versus  $e_2$  plot.

A very bright star ( $\sim 9$ th mag in  $r$ ) is located near the cluster center ( $\sim 2'$  southwest of A1240N-BCG; see Figure 6(a)). Its reflection patterns and circular ghost rings make SExtractor detect numerous spurious objects around it, which also prevents us from identifying real galaxies in the region. Since the artifact is roughly axisymmetric in our coadd mainly because of the field rotation among visits, we modeled the feature as a function of radius from the star and subtracted the model from the coadd. Then, we ran SExtractor a second time on the star-subtracted image and measured the source galaxy shapes that were hidden in the original coadd. We visually inspected every source galaxy in this region, and a source was discarded if its shape was likely to be affected by subtraction residuals.

The objects in our final source catalog are shown as a green Hess diagram with square-root scaling in Figure 4. The mean number density is  $\sim 43 \text{ arcmin}^{-2}$  in the central  $27' \times 27'$  region, where we perform our WL analysis.

Equations (3) and (4) show that the convergence  $\kappa$  is a function of the angular diameter distance ratio  $D_{ls}/D_s$ . This dependence indicates that quantitative interpretation of the observed lensing signal relies on prior knowledge of the source redshift distribution. As mentioned above, we relied on the redshift–magnitude–color relation and utilized the external photometric redshift catalog as a reference to infer source redshifts in our cluster field. A potential concern in this approach is that the redshift–magnitude–color relation in the reference field is significantly different from the one in our source population. Jee et al. (2014) investigated this issue of cosmic variance on their mass determination using the Ultra Deep Field (UDF) and GOODS photometric redshift catalogs of Coe et al. (2006) and Dahlen et al. (2010), respectively. Despite the large difference in field size, they found that the impact of the variance is small in mass estimation, quoting  $\lesssim 4\%$ , which is sufficiently smaller than the statistical uncertainties. In this study, we used the UVUDF catalog of Rafelski et al. (2015), who improved the result of Coe et al. (2006) with the addition of WFC3 IR imaging data.

We account for the differences in depth and filter between the UVUDF and our data as follows. Photometric transformation of the Hubble Space Telescope’s Advanced Camera for Surveys system to the Subaru system was performed with the spectral energy distribution templates in Benítez et al. (2004) and the best-fit photo- $z$  values. We then applied our source selection criteria described above to this transformed UVUDF catalog. We compared the magnitude distribution of this catalog to that of our sources and verified that the two results are consistent up to  $r \lesssim 25.5$ . Beyond the threshold  $r \gtrsim 25.5$ , our source catalog has gradually fewer objects per magnitude bin because of the shallower depth. Assuming that the color–magnitude–redshift relation in UVUDF is valid in our cluster field, we estimated the redshift distribution of our source galaxies after taking the difference in this magnitude distribution (completeness correction) into account.

The lensing efficiency  $\beta$  is defined as

$$\beta = \left\langle \max \left[ \frac{D_{ls}}{D_s}, 0 \right] \right\rangle, \quad (14)$$

where we set  $\beta$  to zero for nonbackground sources, which do not contribute to the lensing signal. We obtained  $\langle \beta \rangle = 0.731$ , and this corresponds to the effective redshift  $z_{\text{eff}} = 0.868$ . Since the lensing efficiency is nonlinear, the use of a single source plane at  $z_{\text{eff}} = 0.868$  produces biased results. The first-order correction (Seitz & Schneider 1997; Hoekstra et al. 2000) is

$$g' = \left[ 1 + \left( \frac{\langle \beta^2 \rangle}{\langle \beta \rangle^2} - 1 \right) \kappa \right] g, \quad (15)$$

where  $g'$  is the uncorrected reduced shear. We obtained  $\langle \beta^2 \rangle = 0.579$ , which reduces the observed shear  $g'$  by a factor of  $(1 + 0.08\kappa)$ .

### 3.2.5. 2D WL Mass Reconstruction

The conversion of the measured ellipticities into the surface mass density ( $\kappa$ ) was performed using the FIATMAP code (Fischer & Tyson 1997), which implements the Kaiser & Squires (1993) method in real space. To investigate the uncertainties in the mass density and peak centroids, we generated 1000 bootstrap realizations, from which we derived the rms map of the convergence field. The FIATMAP convergence map was divided by the rms map to obtain the significance map.

In Figure 10, the convergence significance map is overlaid on the Subaru color-composite image (top left panel), the luminosity-weighted density map (top right panel), and the 52 ks Chandra X-ray surface brightness map (bottom left panel). Our mass reconstruction reveals that A1240 consists of northern and southern mass clumps, which are significant at the  $\sim 7.6\sigma$  and  $\sim 3.3\sigma$  levels, respectively, with a projected separation of  $\sim 1.30$  Mpc. The mass distribution of A1240 is elongated in the north–south direction, resembling the cluster galaxy luminosity distribution (A1240N and A1240S). In addition, the third mass clump collocated with the luminosity peak of A1237 is detected at the  $\sim 4.1\sigma$  level,  $\sim 1.52$  Mpc south of the A1240S mass clump. The  $\sim 68\%$  peak distributions measured from the 1000 bootstrap-resampled mass maps show that all three peaks are in good spatial agreement with the corresponding luminosity peaks. Finally, the WL mass reconstruction detects a bridge connecting A1240 and A1237 at the  $\geq 2\sigma$  level. This filamentary extension in the intercluster region coincides with the overdensities of member galaxies. This is aligned with the  $\sim 80$  Mpc-long filamentary structure in the plane of the sky (see Section 3.1.3).

The Chandra X-ray emission is also stretched in the same orientation as the A1240 mass and galaxies. In the bottom left panel of Figure 10, the X-ray surface brightness map shows a clumpy, elongated structure from which it is somewhat difficult to quantify the exact number of substructures. Nevertheless, it is clear that the gas extent is more compact, i.e., the gas filament is shorter than the baselines formed by the two mass/galaxy clumps, which is consistent with our expectation that A1240 is a postmerger that happened in the north–south direction.

The bottom right panel of Figure 10 presents the WL mass (blue), LOFAR 143 MHz intensity (green; Hoang et al. 2018), and Chandra X-ray surface brightness (red) maps, together with

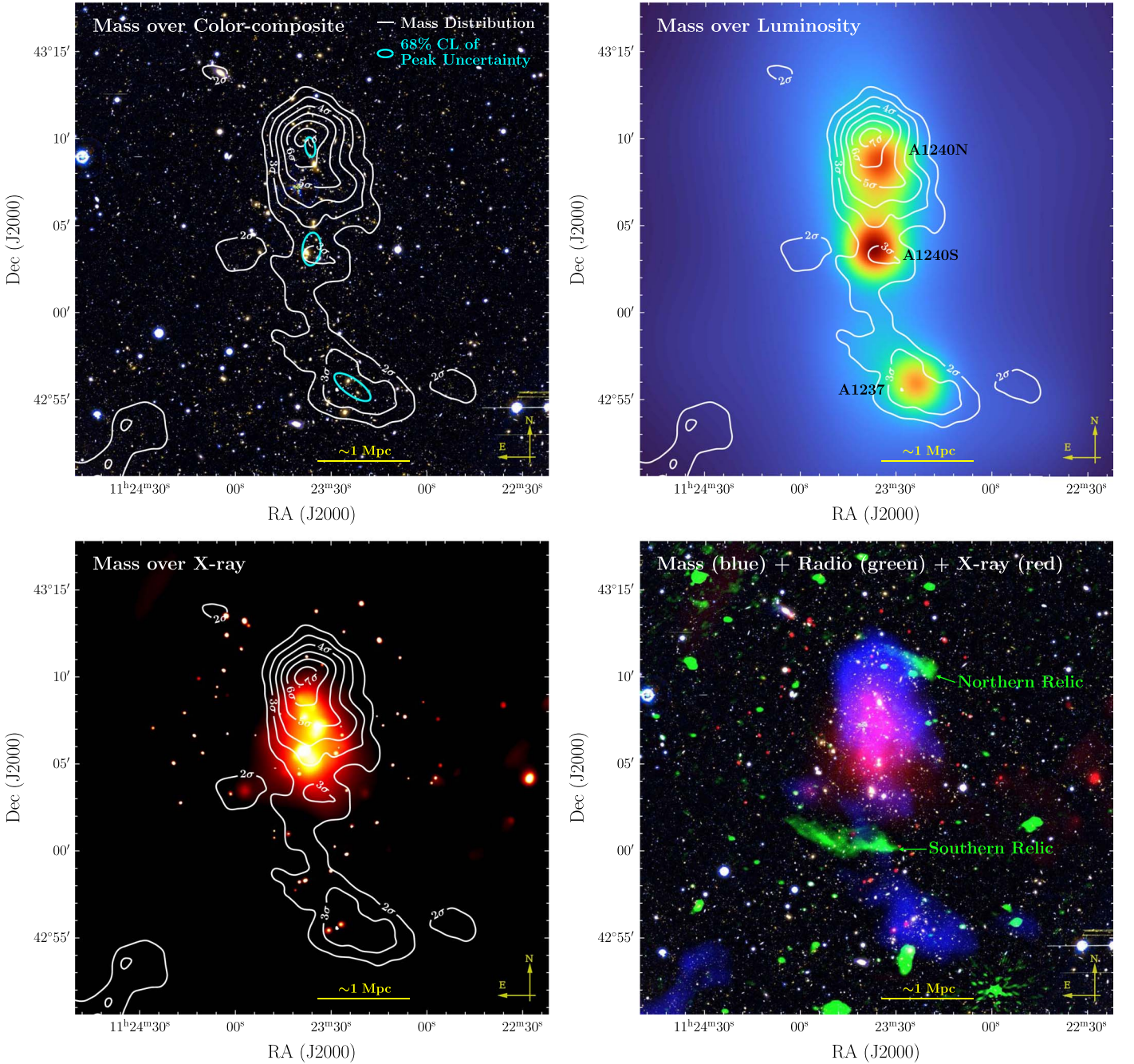


**Figure 10.** Mass reconstruction of the A1240 field. We display our convergence ( $\kappa$ ) significance map, which is obtained from division of the convergence map by the rms map. The rms is determined from 1000 bootstrapping runs. The lowest contour corresponds to the  $2\sigma$  significance. We overlay the linearly spaced significance contours on the Subaru color-composition image (top left), the galaxy luminosity-weighted density map (top right), and the 52 ks Chandra image (bottom left; only available for A1240). In the top left panel, the 68% covariance confidence limits of the mass centroid uncertainties are marked with cyan ellipses. The composite image shown in the bottom right panel shows the mass, LOFAR 143 MHz radio (Hoang et al. 2018), and Chandra X-ray data. Our WL mass reconstruction detects three mass clumps associated with the three peaks in the optical luminosity. The A1240N, A1240S, and A1237 peaks are detected at the  $\sim 7.6\sigma$ ,  $\sim 3.3\sigma$ , and  $\sim 4.1\sigma$  levels, respectively. The distribution of the X-ray emission elongated in the north–south direction is approximately cospatial with the optical luminosity. Compared with the mass, the extent of the X-ray emission is compact and mostly confined between the two mass clumps in A1240. The northern and southern radio relics are located near the edges of A1240N and A1240S defined by the optical luminosity.

the Subaru color-composite image. The northern and southern radio relics, which bracket the two substructures of A1240, are stretched in the east–west direction, nearly perpendicular to the hypothesized merger axis. Hoang et al. (2018) found indications of possible discontinuities in X-ray surface brightness at the location of the relics, which is also expected if the radio relics indeed trace the merger shocks.

The southern relic is brighter and longer. Numerical simulations have shown that in general, the kinetic energy flux, which is proportional to the relic brightness, associated with a less massive cluster in the binary collision is larger. Since our WL analysis suggests that A1240S is two to three times less massive (Section 3.2.6), this disparity in relic size is also consistent with our expectation.

As for A1237, since its redshift is similar to that of A1240, an important question is whether it has already interacted with A1240. Hoang et al. (2018) detected a tailed radio galaxy (we denoted it A1237BCG-S in Figure 6(a)). Since it has an extension toward the south, the authors suggested that A1237BCG-S might be moving through the local intracluster medium toward the A1237 center. However, this does not help us to infer the bulk motion of A1237. Since A1237 is not fully covered by the Chandra data, the question still remains unresolved. Nevertheless, from the symmetric X-ray and radio features and the large separation from A1240, our conjecture is that A1237 is not likely to be involved in the recent A1240 north–south merger responsible for the two distinct radio relics and the characteristic X-ray morphology.

### 3.2.6. Mass Estimation

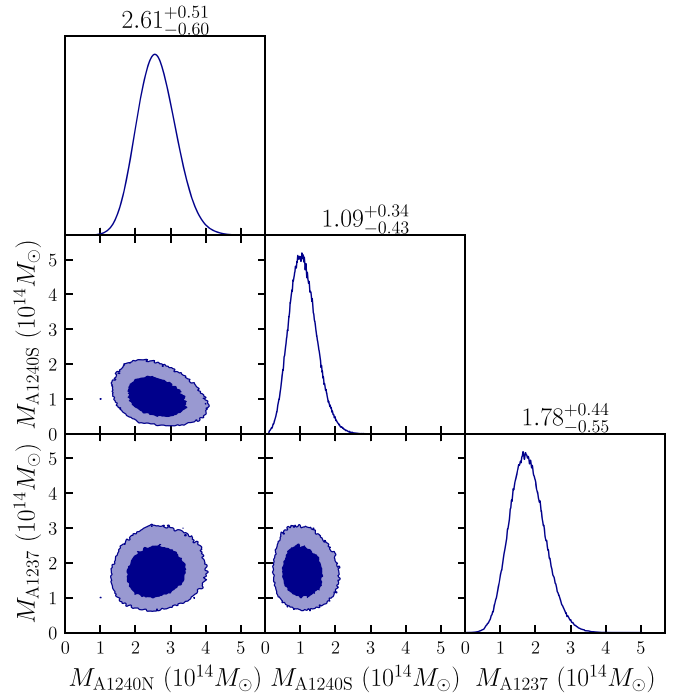
As we detected two mass components in A1240 and a separate clump in A1237, we cannot treat the mass distribution of the A1240 field as a single halo. To quantify the mass of each subcluster, we performed a Markov Chain Monte Carlo (MCMC) analysis by simultaneously fitting three halos. For each halo, we assumed a Navarro–Frenk–White (NFW; Navarro et al. 1996, 1997) profile with the mass–concentration relation of Duffy et al. (2008) and fixed their centroids at the luminosity centers. We excluded source galaxies at the core of each halo located within  $r_{\min} = 10''$ . During the likelihood sampling, we imposed a flat prior on mass with the interval  $10^{13} M_{\odot} < M_{200} < 10^{15} M_{\odot}$ .

Figure 11 shows the MCMC results. The  $M_{200}$  values of the northern and southern halos of A1240 are  $M_{A1240N} = 2.61^{+0.51}_{-0.60} \times 10^{14}$  and  $M_{A1240S} = 1.09^{+0.34}_{-0.43} \times 10^{14} M_{\odot}$ , respectively, which shows that A1240 is a merger with a mass ratio of  $\sim 2:1$ . We also estimated A1237’s mass to be  $M_{A1237} = 1.78^{+0.44}_{-0.55} \times 10^{14} M_{\odot}$ . The mass estimation results are summarized in Table 2 and utilized for our merger scenario reconstruction in Section 4.2.

To estimate the A1240 total system mass, we adopted the approach described in Jee et al. (2014). We assumed that the global center of A1240 is the geometric mean of the A1240N and A1240S luminosity peaks. Then, the 3D mass distribution of the entire system is modeled as a superposition of two NFW profiles. For each MCMC sample, we numerically determined the radius from the global center that encloses  $M_{200}$ . The resulting A1240 system mass is  $M_{200} = (4.37 \pm 0.77) \times 10^{14} M_{\odot}$  with  $r_{200} = 1.47 \pm 0.09$  Mpc. Since many previous studies quoted the A1240 mass using  $M_{500}$ , it is also useful to compute  $M_{500}$  with our WL result for a fair comparison. The result is  $M_{500} = (2.83 \pm 0.50) \times 10^{14} M_{\odot}$ . However, since this  $M_{500}$  value is reached at  $r \sim 0.9$  Mpc, which is less than the distance between A1240N and A1240S, we believe that this  $M_{500}$  value does not adequately represent the global property of A1240.

## 4. Discussion

Both identification and quantification of the A1240 substructures based on our multiwavelength studies are critical in our reconstruction of the merging scenario. Here we compare our key measurements with previous studies and present our merging scenario reconstruction.



**Figure 11.** Posterior distributions for the masses of the A1240 northern (A1240N) and southern (A1240S) subclusters and A1237 from MCMC analysis. While fitting three halos with NFW profiles simultaneously, we assumed the Duffy et al. (2008) mass–concentration relation based on the flat  $\Lambda$ CDM cosmology. The filled contours show 68% and 95% confidence limits for marginalized constraints, evaluated from the MCMC chains using the GetDist code (Lewis 2019).

## 4.1. Comparison with Previous Studies

### 4.1.1. Kinematics Comparison

The kinematical properties of the two subclusters in A1240 were studied by B09 and G19b. Using BCGs as tracers of merging subclumps, B09 reported that the LOS rest-frame velocity difference between the northern and southern subclumps is  $\sim 390$  km s $^{-1}$ , which is consistent with the value estimated by G19b ( $394 \pm 117$  km s $^{-1}$ ). However, we obtained a relatively small difference ( $83 \pm 185$  km s $^{-1}$ ) from the nearby member galaxies around the BCGs (Section 3.1.2). A small LOS velocity difference indicates that the merger might be happening close to the plane of the sky and/or that A1240N and A1240S might be observed near their apocenters (e.g., Dawson et al. 2015; Golovich et al. 2016; van Weeren et al. 2017). The  $\sim 2\sigma$  discrepancy is mainly due to the subcluster membership assignment. We only considered the objects in the dense core regions within  $\sim 0.5$  Mpc from the center of each luminosity density peak, whereas previous studies covered an area up to nine times larger. Since the two subclusters are close ( $\sim 1$  Mpc), while the merger is expected to cause significant outflows of the member galaxies, we argue that our conservative choice is safer in the membership identification.

Looking only at the subcluster cores, we find that our result is in agreement with B09, who also found that the inner regions of their subclusters seem to have similar velocities (see their Figures 9 and 10). Their velocity profile for the member galaxies of A1240N gradually increases outward, regardless of the choice of the subcluster center. B09 suggested that perhaps a few galaxies at higher redshift in the outer region of the northern cluster lead to the relatively high mean redshift of

A1240N (thus, a large LOS velocity difference). The projected locations of these galaxies correspond to the candidate cluster GMBCG J170.88991+43.24646 (GMBCG170.89)—the northern yellow star inside the green dashed-dotted circle in the right panel of Figure 8—at a slightly higher redshift than that of A1240. GMBCG170.89 appears to be part of the north–south filamentary structure. The presence of these galaxies could be interpreted as either a group of galaxies possibly accreting onto A1240 through the filament or a plume of outflowing galaxies at large clustercentric distances due to the recent merging event between A1240N and A1240S (as suggested for A1758 by, e.g., Boschin et al. 2012, Schellenberger et al. 2019; A3266 by Quintana et al. 1996, Flores et al. 2000; and Cl0024+1654 by Czoske et al. 2002).

B09 provided the first measurements of the LOS velocity dispersions for the two individual subclusters in A1240 using 32 and 27 member redshifts, respectively. They quoted  $709^{+88}_{-83}$   $\text{km s}^{-1}$  ( $991^{+149}_{-83}$   $\text{km s}^{-1}$ ) for A1240N (A1240S). With a factor of  $\sim 2$  more redshifts, G19b reported that both subclusters have similar velocity dispersions ( $706 \pm 52$  and  $727 \pm 68$   $\text{km s}^{-1}$  for A1240N and A1240S, respectively). Considering only 45 (51) members in the core region of A1240N (A1240S), we obtained  $909 \pm 116$   $\text{km s}^{-1}$  ( $841 \pm 109$   $\text{km s}^{-1}$ ). These velocity dispersions cannot be used as reliable mass proxies because the merger must have made the system depart from the dynamical equilibrium; when we convert our WL measurement to a velocity dispersion under the assumption of a singular isothermal sphere (SIS), we obtain  $540^{+50}_{-55}$   $\text{km s}^{-1}$  ( $464^{+55}_{-63}$   $\text{km s}^{-1}$ ) for A1240N (A1240S), which is significantly lower than the spectroscopic value.

#### 4.1.2. Mass Comparison

The quoted uncertainties of our mass estimates include the statistical contributions from the intrinsic shape noise and ellipticity measurement errors. There are additional systematic uncertainties to keep in mind as one interprets our results. As noted in Jee et al. (2014), scatter in the mass–concentration relation, halo triaxiality, departure from the NFW assumption, and uncorrelated large-scale structures along the LOS can increase the total mass uncertainty up to  $\sim 30\%$ .

Figure 12 summarizes the comparison of the total mass estimates  $M_{500}$  and  $M_{200}$  of A1240 in the literature with our WL results. The first mass estimation of A1240 is presented in B09 based on velocity dispersion measurements. Under the assumption of dynamical equilibrium, they quoted  $M_{\text{vir}} = (0.9\text{--}1.9) \times 10^{15} M_{\odot}$  within  $r_{\text{vir}} = 1.9\text{--}2.4$  Mpc for the entire A1240 system. The B09 result is significantly larger than our WL estimate of the total mass,  $(4.37 \pm 0.77) \times 10^{14} M_{\odot}$  (Section 3.2.6). Possible causes of this large discrepancy were discussed by Pinkney et al. (1996) and Takizawa et al. (2010), who investigated the dependence of the mass prediction through virial theorem on the merger status using numerical simulations of head-on binary mergers. They concluded that the cluster mass estimation through the virial theorem would be severely affected by the merger. The bias is caused not only by the departure from the equilibrium but also by the viewing angle of the merger. For example, according to Pinkney et al. (1996), when a 3:1 mass ratio merger is viewed within  $\sim 60^{\circ}$  of the LOS, the virial mass will be overestimated by up to a factor of 2. Similarly, Takizawa et al. (2010) showed that when a merger is observed along the LOS, a factor of 2 or more overestimation could occur.

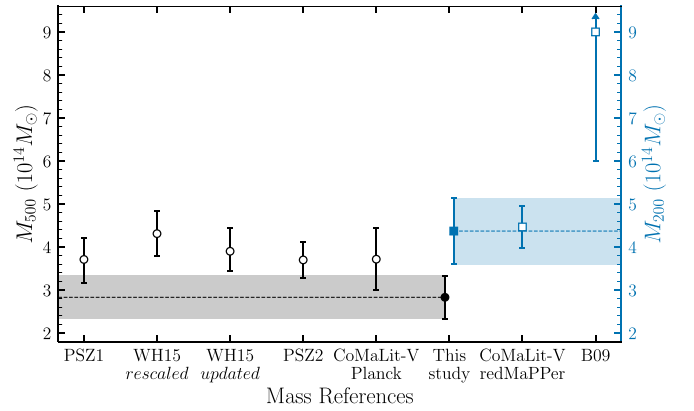


**Figure 12.** The A1240 WL mass comparison with other estimates. Black circles and blue squares are  $M_{500}$  (read the y-axis on the left) and  $M_{200}$  (read the y-axis on the right), respectively, in units of  $10^{14} M_{\odot}$ . Filled symbols (and dashed lines) and shaded regions indicate our mass estimates and the corresponding  $1\sigma$  uncertainties, respectively, from the current WL study. Overall, our results are broadly consistent with previous studies in both  $M_{500}$  and  $M_{200}$ . Note that for the WL evaluation of  $M_{500}$ , our choice of the cluster center (i.e., the geometric center between A1240N and A1240S) may cause underestimation because the mass density is low there. See text for abbreviated names of mass references.

Using the richness–mass ( $\lambda$ – $M_{200}$ ) relation, Sereno & Ettori (2017; abbreviated “CoMaLit-V redMaPPer” in Figure 12) performed mass forecasting of A1240. They used the subset of “Literature Catalogues of weak Lensing Clusters of galaxies” (Sereno 2015) compiled from the WL masses of galaxy clusters in the literature that have counterparts in the SDSS redMaPPer catalog as a calibration sample to obtain the median scaling relation. The resulting mass estimate  $M_{200} = (4.47 \pm 0.50) \times 10^{14} M_{\odot}$  is in good agreement with our WL result.

Planck Collaboration et al. (2015, 2016), who referred to A1240 as PSZ1 G165.41+66.17 and PSZ2 G165.46+66.15, respectively, estimated  $M_{500}$  to be  $M_{\text{PSZ1}} = 3.71^{+0.50}_{-0.54} \times 10^{14}$  and  $M_{\text{PSZ2}} = 3.70^{+0.41}_{-0.42} \times 10^{14} M_{\odot}$  based on the SZ signal. Wen & Han (2015; abbreviated “WH15” in Figure 12) quoted a mass of  $M_{500,\text{rescaled}} = (4.31 \pm 0.52) \times 10^{14} M_{\odot}$  with their calibrated optical mass proxy; their updated richness  $R_{L*,500} = 65.45$  of A1240 can be converted into the mass of  $M_{500,\text{updated}} = 3.90^{+0.54}_{-0.47} \times 10^{14} M_{\odot}$ . The mass estimate of A1240 in Sereno & Ettori (2017; abbreviated “CoMaLit-V Planck” in Figure 12) is  $M_{500} = (3.72 \pm 0.72) \times 10^{14} M_{\odot}$ . Our WL estimate,  $M_{500} = (2.83 \pm 0.50) \times 10^{14} M_{\odot}$ , is marginally consistent with the above, although we believe that our choice of the cluster center biases the measurement lower (see the caveat mentioned in Section 3.2.6).

For the northern and southern subclusters individually, B09 obtained  $M_{\text{vir}} = (5 \pm 2) \times 10^{14}$  and  $(14 \pm 5) \times 10^{14} M_{\odot}$ , respectively, from their LOS velocity dispersion measurements. According to B09, A1240S is about three times more massive. However, when Wittman et al. (2018) used the G19b values of the subcluster velocity dispersion, they obtained similar masses [ $M_{\text{A1240N}} = (4.19 \pm 0.99) \times 10^{14}$  and  $M_{\text{A1240S}} = (4.58 \pm 1.40) \times 10^{14} M_{\odot}$ ]. Our WL mass estimation reveals that the mass ratio is about 2:1 ( $M_{200}^{\text{A1240N}} = 2.61^{+0.51}_{-0.60} \times 10^{14}$  and  $M_{200}^{\text{A1240S}} = 1.09^{+0.34}_{-0.43} \times 10^{14} M_{\odot}$ ). Because the southern radio relic is significantly larger than the northern one, this 2:1 mass ratio better agrees with our understanding that, in general, the kinetic energy flux associated with the less massive system is greater.

## 4.2. Merging Scenario

Cluster mergers happen on a timescale of a few gigayears, while we only witness a single snapshot. To utilize a cluster merger as a useful astrophysical laboratory, it is essential to constrain the stage of the merger, which is often represented by parameters such as time since collision (TSC), collision velocity, viewing angle, impact parameter, apocenter position, etc. Although one of our ultimate goals in MC<sup>2</sup> is to reproduce many observed features with sophisticated high-resolution numerical simulations (e.g., Lee et al. 2020), finding the optimal combination of simulation setups is still a very challenging task limited by severe degeneracies among different parameters and huge computational time. Here we employ the Monte Carlo Merger Analysis Code (MCMAC; Dawson 2013, 2014), which enables fast prediction of the 3D configurations of a cluster merger based on observed features and Monte Carlo simulations.

The MCMAC method employs several assumptions in its analysis of the merger dynamics. They include mass and energy conservation and zero angular momentum throughout the merger history. Thus, each subcluster maintains a constant mass (i.e., input mass from observation). Furthermore, subclusters interact only through gravity. Since the model treats the merger dynamics as an isolated, collisionless, binary system, the effects of the surrounding large-scale structure, dynamical fraction, and tidal stripping of DM and gas are ignored. Despite these caveats, in general, the MCMAC method achieves a good ( $\sim 10\%$ ) accuracy in estimating some important dynamical parameters when compared with hydrodynamic  $N$ -body simulation results (Dawson 2013). A recent study by Kim et al. (2021), however, showed that the MCMAC code produces severely biased results when applied to the ‘‘El Gordo’’ merging cluster, where the dynamical friction is no longer negligible because of the extreme masses of individual subclusters. Fortunately, the moderate mass of A1240 makes the omission of the dynamical friction in MCMAC much less critical in our merging scenario analysis.

The key input parameters to MCMAC are the redshifts and masses of A1240N and A1240S, the projected separation between the two, and their measurement uncertainties. The MCMAC output includes collision velocity, viewing angle, and TSC for each combination of the randomized (within their measurement uncertainties) masses, redshifts, and projected separation. The degeneracies among the output parameters can be reduced by additional constraints, such as the polarization fraction and positions of radio relics. Hoang et al. (2018) measured the mean fractional polarization of A1240N and A1240S to be  $32\% \pm 4\%$  and  $17\% \pm 4\%$ , respectively, from the VLA 2–4 GHz data. We translated these measurements into the viewing angle prior  $\alpha < 51^\circ$ , where  $\alpha$  is the angle between the merger axis and the plane of the sky. In order to utilize the observed relic positions to further constrain the merger state, we need to model the propagation of the relic. Numerical simulations have shown that the merger shock propagation velocity  $v_{\text{relic}}$  (with respect to the center of mass, CM) is related to the associated subcluster collision velocity  $v_{\text{col}}^{\text{CM}}$  (with respect to the CM) at pericenter via  $v_{\text{relic}} \sim \eta v_{\text{col}}^{\text{CM}}$ , where  $\eta$  is close to unity (e.g., Springel & Farrar 2007; Paul et al. 2011), although the exact value is unknown. We adopt  $\eta = 0.9$  as the fiducial value in this paper, following Ng et al. (2015).

Figure 13 shows the probability density functions (PDFs) of the radio-relic positions obtained from the MCMAC result. For

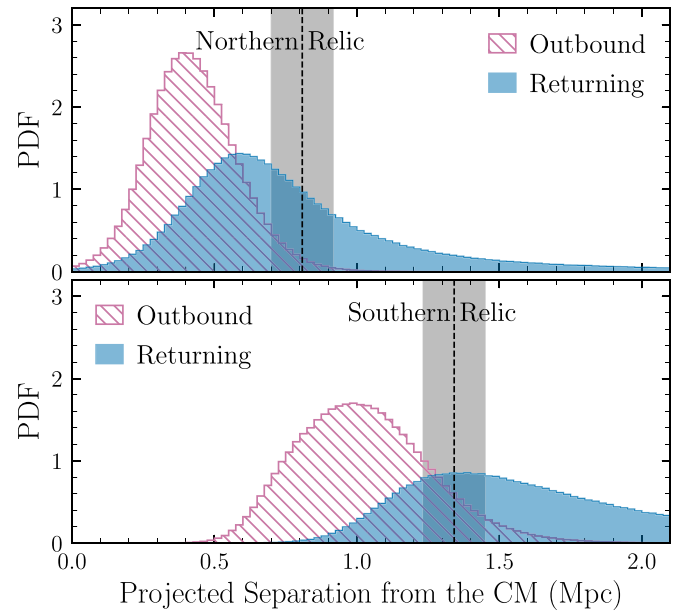


**Figure 13.** The PDFs of the projected separation of the merger shock from the CM. The vertical dashed lines and gray shaded regions indicate the observed locations and positional uncertainties of the radio relics, respectively. The relic positional uncertainties are dominated by the CM positional uncertainties, which are in turn affected by the mass uncertainties. The northern relic favors a returning scenario with  $p_r/p_o \sim 4.9$ , where  $p_r$  and  $p_o$  are the probabilities of the returning and outbound cases, respectively, integrated over the relic position prior interval (top). On the other hand, the difference is small ( $p_r/p_o \sim 1.3$ ) with the southern relic (bottom). Combining the results from both panels (counting the Monte Carlo samples satisfying both constraints), we obtain  $p_r/p_o \sim 37.5$ , which shows that the returning scenario is strongly preferred.

the northern relic, the observed relic position favors a returning scenario ( $p_r/p_o \sim 4.9$ ), whereas the difference is small ( $p_r/p_o \sim 1.3$ ) with the southern relic. When we combine the constraints from both relics (by counting the MCMAC samples that satisfy both relic positions), a returning scenario is strongly favored with  $p_r/p_o \sim 37.5$ .

We compare the viewing angle, collision velocity, and TSC for different priors in Figure 14. For the returning case, when we employ both polarization and radio-relic position priors, the viewing angle, collision velocity, and TSC are constrained to be  $\alpha = 31.4_{-14.9}^{+13.3^\circ}$ ,  $v_{3\text{D},\text{col}} = 1627_{-96}^{+115}$  km s<sup>-1</sup>, and TSC =  $1.68_{-0.15}^{+0.22}$  Gyr, respectively. Although we find that consistent results are obtained for different choices of priors, the differences in uncertainty are significant. For example, when no prior is used, the uncertainty of the TSC increases by a factor of  $\sim 6$  compared to the case when both polarization and radio-relic position priors are used. For the outbound case, which is not favored by the radio-relic position, the collision velocities are similar to the results in the returning case. Interestingly, in this scenario, the most probable viewing angle is somewhat large ( $\alpha \gtrsim 45^\circ$ ) with the polarization and radio-relic priors. We believe that this happens because the projected shock propagation speed must be substantially lowered in order to match the observed relic positions; in this case, the resulting TSC should also be made even longer than the value in the returning case.

Note that our merger scenario is different from that of Wittman (2019), who investigated the dynamical properties of A1240 with simulated analogs and reported that an outbound case is more probable (84% versus 16%). Although the method

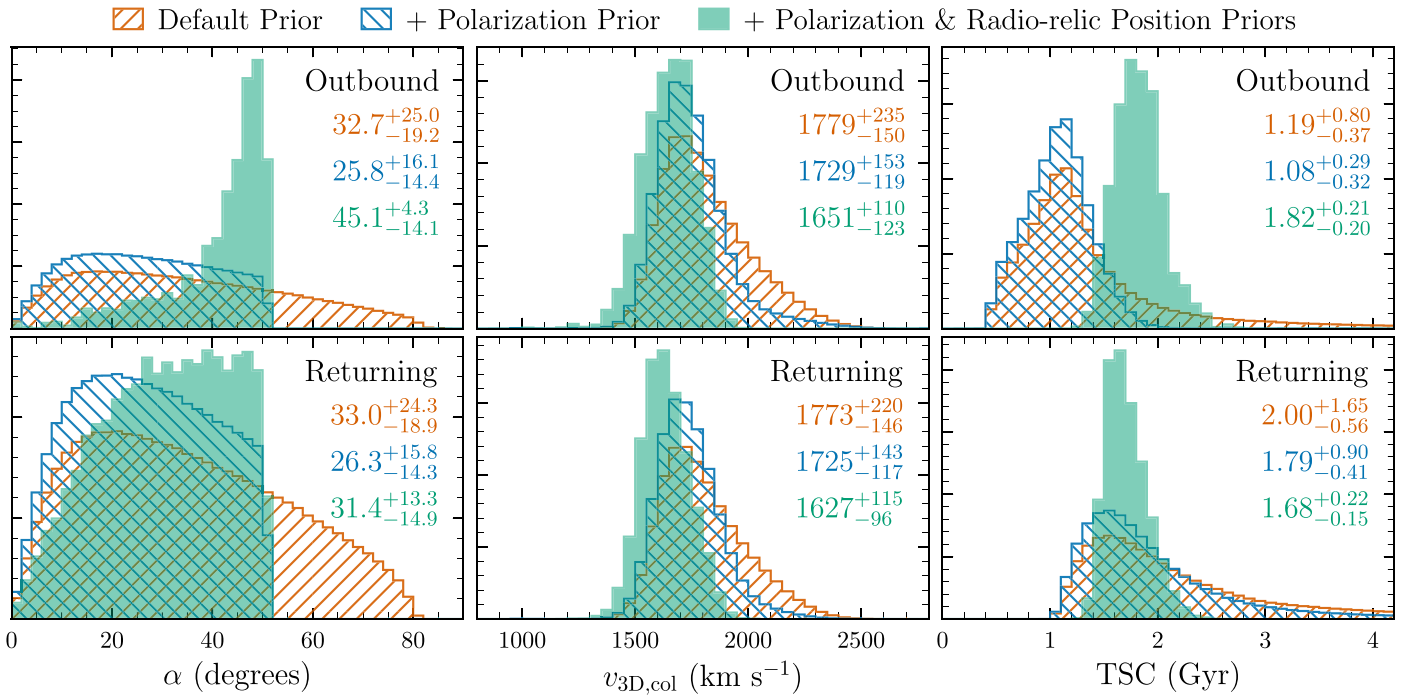


**Figure 14.** Marginalized PDFs of the A1240 merger parameters. With different choices of priors, we display the results for  $\alpha$ , the merger axis angle with respect to the plane of the sky;  $v_{3D,col}$ , the 3D relative velocity at the pericenter; and the TSC for the outbound (top) and returning (bottom) cases.

is different from ours, the discrepancy arises mostly from the fact that Wittman (2019) adopted larger masses ( $\sim 4.2 \times 10^{14}$  and  $\sim 4.6 \times 10^{14} M_{\odot}$  for A1240N and A1240S, respectively) inferred from the subcluster velocity dispersions and also did not use the radio-relic position constraint. For example, the 68% collision velocity interval (1979–2466 km s $^{-1}$ ) estimated by Wittman (2019) roughly corresponds to the escape velocity of the A1240 system computed with the current WL masses.

## 5. Conclusions

We have studied the double radio-relic cluster A1240 and its companion cluster A1237 with multiwavelength data. Our findings are summarized as follows.

1. Our MMT/Hectospec observation increases the number of spectroscopic members to 432, which is a factor of  $\sim 3$  larger than the previous value. Combining the result with our Subaru-based photometric data, we were able to identify the cluster substructures in unprecedented detail.
2. Our Subaru-based WL analysis detects three significant mass clumps with masses of  $M_{A1240N} = 2.61^{+0.51}_{-0.60} \times 10^{14}$ ,  $M_{A1240S} = 1.09^{+0.34}_{-0.43} \times 10^{14}$ , and  $M_{A1237} = 1.78^{+0.44}_{-0.55} \times 10^{14} M_{\odot}$  forming an  $\sim 4$  Mpc filamentary structure in the north–south orientation. These three mass peaks are in good spatial agreement with the cluster galaxy distributions obtained with our spectroscopic and photometric member catalog.
3. The northern (A1240N) and middle (A1240S) mass clumps separated by  $\sim 1$  Mpc are associated with A1240 and collocated with the X-ray emission detected with the Chandra data. The double radio relics bracket the edges of these two subclusters.
4. Our Monte Carlo analysis shows that the current positions of the double radio relics strongly constrain

the merger phase, favoring a returning scenario with TSC  $\sim 1.7$  Gyr.

5. With the SDSS DR16 data analysis, we find that A1240 is embedded in the much larger scale ( $\sim 80$  Mpc) filamentary structure whose orientation is in remarkable agreement with the hypothesized merger axis of A1240.

Radio relic clusters are receiving growing attention as powerful astrophysical laboratories that enable useful experiments to probe the properties of DM, mechanisms of cosmic-ray particle acceleration, evolution of plasma turbulence, etc., which are impossible on the ground. The rarest of the relic classes are the symmetric double relics, which are equidistant from the cluster center with comparable surface brightness and provide two redundant probes of the same merger. To date, about six objects that meet our criteria have been reported, and A1240 is one of the cleanest systems that exhibit a distinct bimodal mass structure. One important future scientific objective of our MC $^2$  project is to follow up these priority targets with high-fidelity numerical simulations and address the aforementioned scientific questions. Our multiwavelength study of A1240 presented here serves as a principal stepping stone to this goal.

This work was supported by the K-GMT Science Program (PID: MMT-2019A-004) of the Korea Astronomy and Space Science Institute (KASI). The observations reported here were obtained at the MMT Observatory, a joint facility of the Smithsonian Institution and the University of Arizona. This work is based in part on data collected at the Subaru Telescope and obtained from the SMOKA, which is operated by the Astronomy Data Center, National Astronomical Observatory of Japan. H.C. and K.F. thank Ho Seong Hwang for providing guidance on the MMT/Hectospec data reduction. H.C. acknowledges support from the Brain Korea 21 FOUR Program. M.J.J. acknowledges support for the current research

from the National Research Foundation (NRF) of Korea under programs 2017R1A2B2004644 and 2020R1A4A2002885.

**Facilities:** Subaru(Suprime-Cam), MMT(Hectospec), CXO, LOFAR.

**Software:** Astropy (Astropy Collaboration et al. 2013, 2018), CIAO (Fruscione et al. 2006), emcee (Foreman-Mackey et al. 2013), FIATMAP (Fischer & Tyson 1997), GetDist (Lewis 2019), HSRED (<https://github.com/MMTObservatory/hsred>), IRAF/RVSAO (Kurtz & Mink 1998), Matplotlib (Hunter 2007), MPFIT (Markwardt 2009), MCMAC (Dawson 2014), NumPy (Harris et al. 2020), SCAMP (Bertin 2006), SciPy (Virtanen et al. 2020), SDFRED2 (Ouchi et al. 2004), SExtractor (Bertin & Arnouts 1996), SWarp (Bertin et al. 2002).

### ORCID iDs

Hyejeon Cho  <https://orcid.org/0000-0001-5966-5072>

M. James Jee  <https://orcid.org/0000-0002-5751-3697>

Rory Smith  <https://orcid.org/0000-0001-5303-6830>

Kyle Finner  <https://orcid.org/0000-0002-4462-0709>

Wonki Lee  <https://orcid.org/0000-0002-1566-5094>

### References

- Abell, G. O. 1958, *ApJS*, **3**, 211
- Abell, G. O., Corwin, H. G. J., & Olowin, R. P. 1989, *ApJS*, **70**, 1
- Astropy Collaboration, Price-Whelan, A. M., Sipőcz, B. M., et al. 2018, *AJ*, **156**, 123
- Astropy Collaboration, Robitaille, T. P., Tollerud, E. J., et al. 2013, *A&A*, **558**, A33
- Barrena, R., Girardi, M., Boschin, W., & Dasí, M. 2009, *A&A*, **503**, 357
- Bartelmann, M., & Schneider, P. 2001, *PhR*, **340**, 291
- Beers, T. C., Flynn, K., & Gebhardt, K. 1990, *AJ*, **100**, 32
- Benítez, N., Ford, H., Bouwens, R., et al. 2004, *ApJS*, **150**, 1
- Bernstein, G. M. 2010, *MNRAS*, **406**, 2793
- Bertin, E. 2006, in ASP Conf. Ser., 351, Astronomical Data Analysis Software and Systems XV, ed. C. Gabriel et al. (San Francisco, CA: ASP), 112
- Bertin, E., & Arnouts, S. 1996, *A&AS*, **117**, 393
- Bertin, E., Mellier, Y., Radovich, M., et al. 2002, in ASP Conf. Ser., 281, Astronomical Data Analysis Software and Systems XI, ed. D. A. Bohlender, D. Durand, & T. H. Handley (San Francisco, CA: ASP), 228
- Bonafede, A., Giovannini, G., Feretti, L., Govoni, F., & Murgia, M. 2009, *A&A*, **494**, 429
- Boschin, W., Girardi, M., Barrena, R., & Nonino, M. 2012, *A&A*, **540**, A43
- Coe, D., Benítez, N., Sánchez, S. F., et al. 2006, *AJ*, **132**, 926
- Czoske, O., Moore, B., Kneib, J. P., & Soucail, G. 2002, *A&A*, **386**, 31
- Dahlen, T., Mobasher, B., Dickinson, M., et al. 2010, *ApJ*, **724**, 425
- David, L. P., Forman, W., & Jones, C. 1999, *ApJ*, **519**, 533
- Dawson, W. A. 2013, *ApJ*, **772**, 131
- Dawson, W. A. 2014, MCMAC: Monte Carlo Merger Analysis Code, Astrophysics Source Code Library, <http://ascl.net/1407.004>
- Dawson, W. A., Jee, M. J., Stroe, A., et al. 2015, *ApJ*, **805**, 143
- de Gasperin, F., Intema, H. T., van Weeren, R. J., et al. 2015, *MNRAS*, **453**, 3483
- de Gasperin, F., van Weeren, R. J., Brüggén, M., et al. 2014, *MNRAS*, **444**, 3130
- Duffy, A. R., Schaye, J., Kay, S. T., & Dalla Vecchia, C. 2008, *MNRAS*, **390**, L64
- Enßlin, T. A., Biermann, P. L., Klein, U., & Kohle, S. 1998, *A&A*, **332**, 395
- Fabricant, D., Fata, R., Roll, J., et al. 2005, *PASP*, **117**, 1411
- Feretti, L., Giovannini, G., Govoni, F., & Murgia, M. 2012, *A&ARv*, **20**, 54
- Finner, K., HyeonHan, K., Jee, M. J., et al. 2021, *ApJ*, **918**, 72
- Finner, K., Jee, M. J., Golovich, N., et al. 2017, *ApJ*, **851**, 46
- Fischer, P., & Tyson, J. A. 1997, *AJ*, **114**, 14
- Flores, R. A., Quintana, H., & Way, M. J. 2000, *ApJ*, **532**, 206
- Foreman-Mackey, D., Hogg, D. W., Lang, D., & Goodman, J. 2013, *PASP*, **125**, 306
- Fruscione, A., McDowell, J. C., Allen, G. E., et al. 2006, *Proc. SPIE*, **6270**, 62701V
- Golovich, N., Dawson, W. A., Wittman, D., et al. 2016, *ApJ*, **831**, 110
- Golovich, N., Dawson, W. A., Wittman, D. M., et al. 2019a, *ApJS*, **240**, 39
- Golovich, N., Dawson, W. A., Wittman, D. M., et al. 2019b, *ApJ*, **882**, 69
- Hao, J., McKay, T. A., Koester, B. P., et al. 2010, *ApJS*, **191**, 254
- Harris, C. R., Millman, K. J., van der Walt, S. J., et al. 2020, *Natur*, **585**, 357
- Harris, W. E. 1990, *PASP*, **102**, 949
- Hoang, D. N., Shimwell, T. W., van Weeren, R. J., et al. 2018, *MNRAS*, **478**, 2218
- Hoekstra, H., Franx, M., & Kuijken, K. 2000, *ApJ*, **532**, 88
- Hunter, J. D. 2007, *CSE*, **9**, 90
- Jee, M. J., Blakeslee, J. P., Sirianni, M., et al. 2007, *PASP*, **119**, 1403
- Jee, M. J., Dawson, W. A., Stroe, A., et al. 2016, *ApJ*, **817**, 179
- Jee, M. J., Hughes, J. P., Menanteau, F., et al. 2014, *ApJ*, **785**, 20
- Jee, M. J., Stroe, A., Dawson, W., et al. 2015, *ApJ*, **802**, 46
- Jee, M. J., & Tyson, J. A. 2011, *PASP*, **123**, 596
- Jee, M. J., Tyson, J. A., Schneider, M. D., et al. 2013, *ApJ*, **765**, 74
- Kaiser, N., & Squires, G. 1993, *ApJ*, **404**, 441
- Kempner, J. C., & Sarazin, C. L. 2001, *ApJ*, **548**, 639
- Kim, J., Jee, M. J., Hughes, J. P., et al. 2021, *ApJ*, **923**, 101
- Kneib, J.-P., & Natarajan, P. 2011, *A&ARv*, **19**, 47
- Koester, B. P., McKay, T. A., Annis, J., et al. 2007, *ApJ*, **660**, 239
- Kurtz, M. J., & Mink, D. J. 1998, *PASP*, **110**, 934
- Lee, W., Jee, M. J., Kang, H., et al. 2020, *ApJ*, **894**, 60
- Lewis, A. 2019, arXiv:1910.13970
- Mandelbaum, R., Rowe, B., Bosch, J., et al. 2014, *ApJS*, **212**, 5
- Markwardt, C. B. 2009, in ASP Conf. Ser., 411, Astronomical Data Analysis Software and Systems XVIII, ed. D. A. Bohlender, D. Durand, & P. Dowler (San Francisco, CA: ASP), 251
- Melchior, P., & Viola, M. 2012, *MNRAS*, **424**, 2757
- Miyazaki, S., Komiyama, Y., Sekiguchi, M., et al. 2002, *PASJ*, **54**, 833
- Monteiro-Oliveira, R., Lima Neto, G. B., Cypriano, E. S., et al. 2017, *MNRAS*, **468**, 4566
- Narayan, R., & Bartelmann, M. 1996, arXiv:astro-ph/9606001
- Navarro, J. F., Frenk, C. S., & White, S. D. M. 1996, *ApJ*, **462**, 563
- Navarro, J. F., Frenk, C. S., & White, S. D. M. 1997, *ApJ*, **490**, 493
- Ng, K. Y., Dawson, W. A., Wittman, D., et al. 2015, *MNRAS*, **453**, 1531
- Ouchi, M., Shimasaku, K., Okamura, S., et al. 2004, *ApJ*, **611**, 660
- Paul, S., Iapichino, L., Miniati, F., Bagchi, J., & Mannheim, K. 2011, *ApJ*, **726**, 17
- Pinkney, J., Roettiger, K., Burns, J. O., & Bird, C. M. 1996, *ApJS*, **104**, 1
- Planck Collaboration, Ade, P. A. R., Aghanim, N., et al. 2015, *A&A*, **581**, A14
- Planck Collaboration, Ade, P. A. R., Aghanim, N., et al. 2016, *A&A*, **594**, A27
- Quintana, H., Ramirez, A., & Way, M. J. 1996, *AJ*, **112**, 36
- Rafelski, M., Teplitz, H. I., Gardner, J. P., et al. 2015, *AJ*, **150**, 31
- Refregier, A., Kacprzak, T., Amara, A., Bridle, S., & Rowe, B. 2012, *MNRAS*, **425**, 1951
- Röttgering, H. J. A., Wieringa, M. H., Hunstead, R. W., & Ekers, R. D. 1997, *MNRAS*, **290**, 577
- Schellenberger, G., David, L., O'Sullivan, E., Vrtilik, J. M., & Haines, C. P. 2019, *ApJ*, **882**, 59
- Schlafly, E. F., & Finkbeiner, D. P. 2011, *ApJ*, **737**, 103
- Seitz, C., & Schneider, P. 1997, *A&A*, **318**, 687
- Serenó, M. 2015, *MNRAS*, **450**, 3665
- Serenó, M., & Etori, S. 2017, *MNRAS*, **468**, 3322
- Springel, V., & Farrar, G. R. 2007, *MNRAS*, **380**, 911
- Takizawa, M., Nagino, R., & Matsushita, K. 2010, *PASJ*, **62**, 951
- Tonry, J., & Davis, M. 1979, *AJ*, **84**, 1511
- van Weeren, R. J., Andrade-Santos, F., Dawson, W. A., et al. 2017, *NatAs*, **1**, 0005
- van Weeren, R. J., de Gasperin, F., Akamatsu, H., et al. 2019, *SSRv*, **215**, 16
- Virtanen, P., Gommers, R., Oliphant, T. E., et al. 2020, *NatMe*, **17**, 261
- Wen, Z. L., & Han, J. L. 2015, *ApJ*, **807**, 178
- Wen, Z. L., Han, J. L., & Liu, F. S. 2012, *ApJS*, **199**, 34
- Wittman, D. 2019, *ApJ*, **881**, 121
- Wittman, D., Cornell, B. H., & Nguyen, J. 2018, *ApJ*, **862**, 160
- Wittor, D., Etori, S., Vazza, F., et al. 2021, *MNRAS*, **506**, 396